STScI | SPACE TELESCOPE SCIENCE INSTITUTE

Instrument Science Report WFC3 2018-16

WFC3/UVIS - Temporal and Spatial Variations in Photometry

Harish Khandrika, Susana Deustua, Jennifer Mack

November 8, 2018

Abstract

We report the results of a study of the Wide Field Camera 3 (WFC3) UVIS detector sensitivity losses since installation in 2009. The study was performed using cosmic-ray cleaned and drizzled observations of the HST white dwarf spectrophotometric standards, GD153, G191B2B, and GD71, and the G-type star P330E. We measure sensitivity changes by taking the ratio of the aperture photometry of the standards to a fiducial value provided by synthetic photometry. We find an overall decrease in sensitivity in both UVIS chips of 0.1% to 0.3% per year. Corrections for sensitivity loss may be manually applied to the computed count-rate values prior to flux calibration in order to correct for the detector sensitivity at the epoch of observation. These are recommended only for comparing "relative" photometry at multiple epochs, since the absolute calibration is limited to 1 to 2 % accuracy. We find that the rate of sensitivity loss in the two UVIS chips are different and require separate corrections.

Introduction

The primary goal of photometric calibration is to accurately convert photon count rates (e.g. electrons per second) into physical units (e.g. $ergs\ sec^{-1}\ cm^{-2}\ \AA^{-1}$). An optical instrument's wavelength dependent system throughput may change and its photometric calibration will not remain constant. Reasons for the change in sensitivity can be attributed to changes in optical coatings and detector quantum efficiency, among others. Therefore, to retain the accuracy of the calibration and deliver consistent photometry, astronomical instruments

require constant recalibration and adjustment. WFC3 calibration images such as flat-fields, biases, and darks are continuously acquired and then applied by the calwf3 data reduction pipeline in order to provide the most accurate calibrated data products. WFC3/UVIS is used for important scientific observations, many of which are acquired at multiple epochs, and it is therefore imperative to compute and track the changes in the sensitivity over time of the WFC3 detectors as they age.

In this report we describe the process of computing and tracking the temporal and spatial changes in WFC3/UVIS photometry using standard star data. We describe the data used in the analysis and detail the methods used to reduce and process the images as well as the protocol for aperture photometry. Finally, we discuss the results and the implications for science observations and general correction of data.

Methods

Description of Data

To measure possible changes in the photometry over time and per detector amplifier, observations in subarray modes of the three HST photometric standard white dwarfs (GD153, GD71, G191B2B) and the G-type (P330E) standard are analyzed. The full list of proposal IDs are listed in Appendix Table A1. Observations, filters, and dates are provided for each star in Appendix Tables A2 (GD71), A3 (G191B2B), A4 (GD153), and A5 (P330E). All four stars were observed in the corner subarrays C512ASUB, C512BSUB, C512CSUB, and C512DSUB to minimize CTE (charge transfer efficiency) effects and to optimize the observation efficiency. Observations with exposure times less than or equal to 1 second are not included in the analysis as these may be affected by the shutter timing (Hilbert, 2009; Sahu, Gosmeyer, and Sylvia Baggett, 2015).

Processing

The calibrated flc.fits[1] files were obtained from MAST (Mikulski Archive for Space Telescopes) and processed with the CALWF3 pipeline using the default parameters for bias subtraction, dark subtraction, flatfield, post-flash and CTE corrections, and for flux (FLUXCORR) corrections (Ryan et al., 2016). Drizzled images (drc.fits) were created with AstroDrizzle from the flc images for each visit (single orbit visits) for each star, filter and subarray combination, to remove cosmic rays and to improve the signal to noise of each target star, and preserve flux. The UVIS chip 2 scaling, to allow it to use the same zero point as UVIS chip 1 (performed via the FLUXCORR switch), is 'backed out' by dividing data taken with UVIS2-C512C-SUB and UVIS2-C512D-SUB by PHTRATIO. This is required for comparison of count-rates with the synthetic photometry.

[1]The extension for CTE corrected data products from CALWF3 is flc.fits

Centroids and photometry

Stellar centroids are found using IDL's implementation of the DAOPHOT CENTROID routine. This was performed on the flc images to ensure that the visit-level data were perfectly aligned (with tweakreg) before drizzling. Since the star's position changes slightly based on visit and after drizzling, centroiding had to be re-performed on the drc images before aperture photometry could be computed. Aperture photometry was computed using the IDL implementation of Stetson DAOPHOT's APER routine (Stetson, 1987), which is more accurate than the Pyraf implementation of DAOPHOT (Bajaj and Khandrika, 2017). The "EXACT" keyword was set when performing aperture photometry to ensure a circular aperture.

A range from 1 to 150 pixels (corresponding to 0.04 to 6 arcseconds) was chosen for the aperture radii and an annulus from 150 to 250 pixels (6 to 10 arcseconds) was chosen for the sky. Photometry was performed on the drc images, and so all flux values are reported in electrons-per-second. The stellar flux is computed using a circular aperture and the sky computed with a circular annulus. The 3-sigma-clipped mean of the sky annulus flux is subtracted from the stellar flux.

We performed photometry using a 10 pixel aperture radius because at this radius, the encircled energy of the star is not significantly affected by 'breathing' or the airy rings (Sabbi and Bellini, 2013). Figure 1 shows the standard deviation (normalized to the mean) of the aperture photometry (count rate) versus aperture radius for all source observations taken in F606W for amplifiers (hereafter amps) A and C. The deviation is higher for the first few aperture radii, decreasing with increasing radius and minimizing within 10 pixels (for chip 1). Beyond 10 pixels, the standard deviation increases with increasing radius as the signal-to-noise declines.

Analysis

Synthetic Photometry

When comparing photometric measurements between different stars at different times, it is useful to have a reference point as a baseline. One option would be to use the first observation as the fiducial measurement point on which to base the rest of the measurements. However, the date of first observation is different for each star and filter, and there is no single point in time common to all stars and filters. Therefore we have chosen to compare the observed photometry with synthetic photometry computed using pysynphot [2] and the latest CALSPEC spectrum (STIS-NICMOS) for each photometric standard. To match the aperture for the standard star observations, synthetic photometry was calculated for an aperture radius of 0.3692 arcseconds (i.e. 10 pixels) for every standard star, filter, and detector combination. For throughputs the TMC and TMG files used were 24u1536nm_tmc.fits and 2381905mm_tmg.fits.

[2] http://pysynphot.readthedocs.io/en/latest/

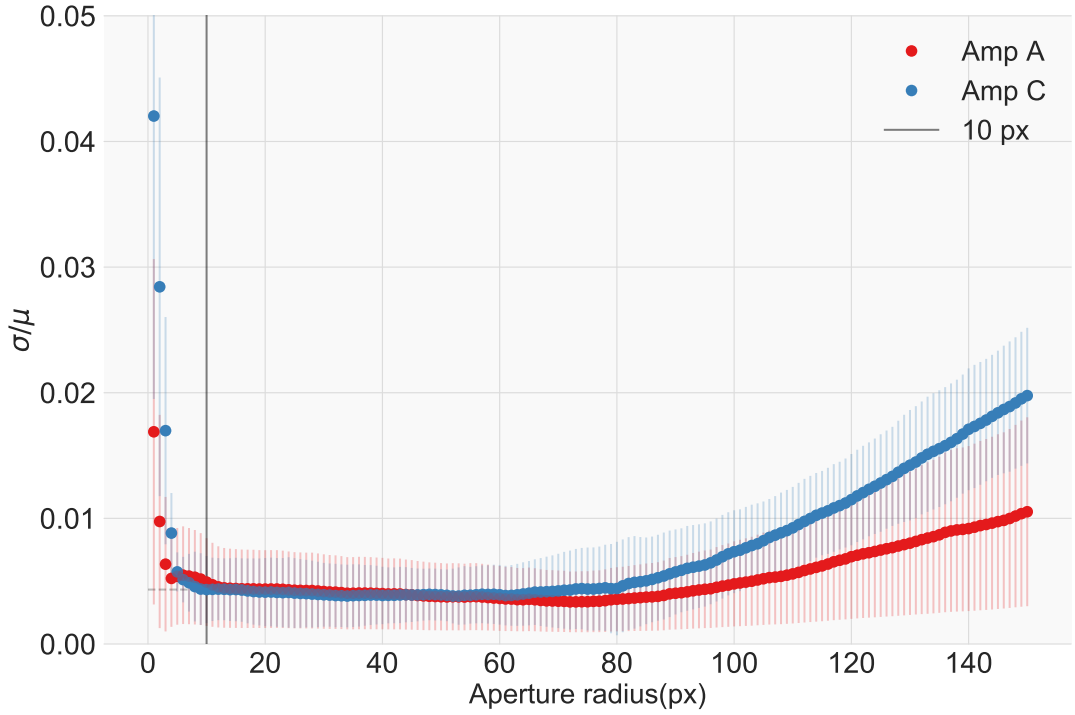

Figure 1: Standard deviation [σ] (normalized by the mean [μ]) of the photometry (count rate) of all stars versus aperture in F606W. The black vertical line marks the 10-pixel aperture.

Linear Fitting

The rate of change in sensitivity with time is determined from the slope of a linear fit to the ratio of observed to synthetic count-rate versus time for each filter and detector. Linear least-square fits were computed, weighting all stars equally after applying sigma-clipping to the data. However, no fit is made when there are fewer than six observations and the time range of observations is less than three years due to insufficient data to accurately constrain the linear fits with high confidence (low error). Because the flat-field calibration is imperfect near the edges of the CCDs (Mack, Rajan, and Bowers, 2015), i.e., where the data for the photometry calibration programs are obtained, each amplifier is fit separately and a constant offset is applied to the photometry to match the amps on a given CCD. The photometry is separated by chip, where Chip 1 includes observations in Amps A and B and Chip 2 includes observations in Amps C and D for the four stars. GD153 and P330E observations were the primary calibration standards shortly after launch, and the other standards were added in later calibration programs.

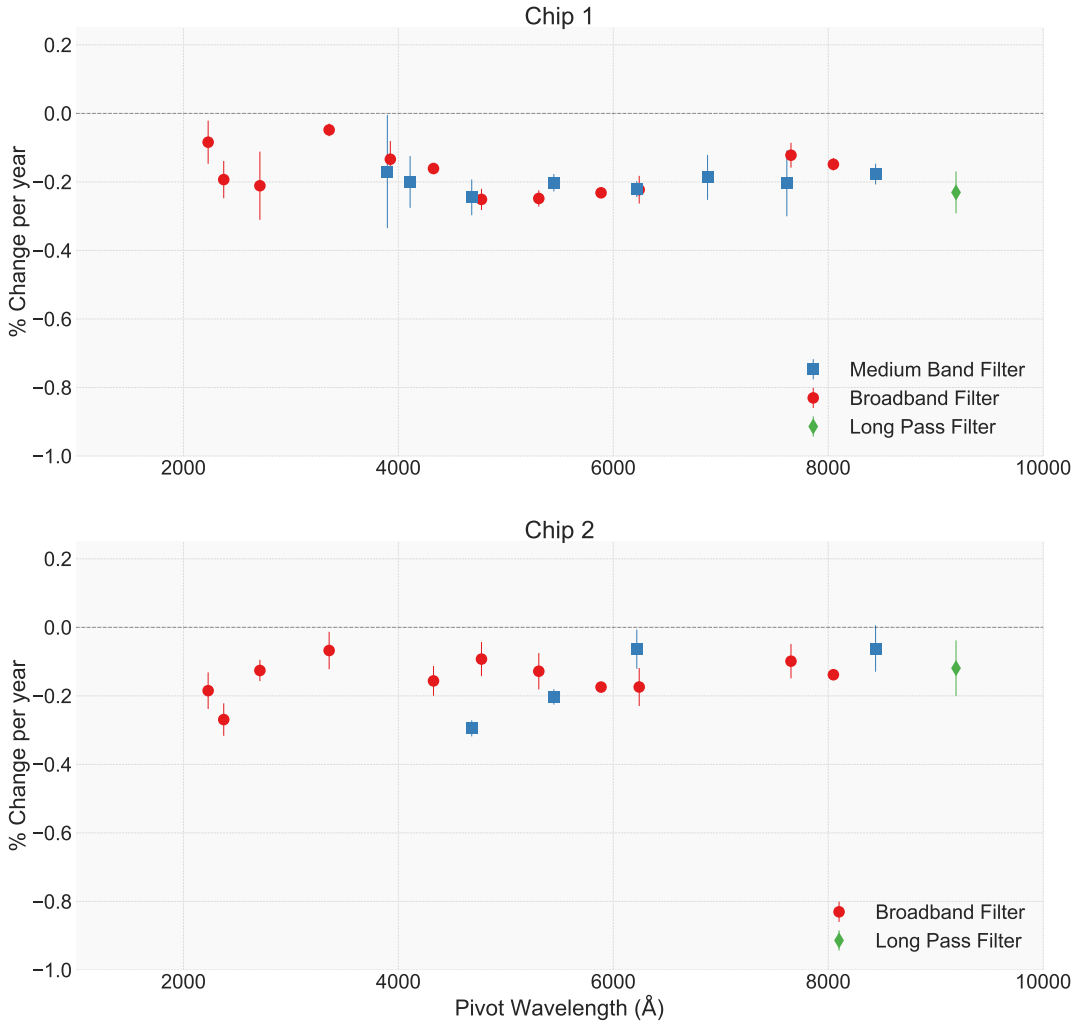

Figure 2: The percent change in the detector sensitivity (computed for all sources) per year versus pivot wavelength for the filter used. The pivot wavelength is the effective wavelength of a filter calculated based on the integrated system throughput (Tokunaga and Vacca, 2005). The top and bottom figures are for Chip 1 and Chip 2 (all amps). Red circles represent the wide-band filters, blue squares represent the medium band filters, and green diamond represents the F850LP filter.

Results and Discussion

Sensitivity Losses with Time

Figures A1 through A21 in the appendix show the change in sensitivity over time as years since WFC3's installation in HST on May 11, 2009 (MJD 54962), for each filter as a function

of the observed to synthetic flux (count-rate) ratio. We find that for amplifiers on the same detector the measured flux is typically within 1% (mean $\sim$ 0.5%) but can differ by up to 2%. These offsets are due to imperfections in the flat fields at the corners as previously mentioned. However, the fitted slopes for amps on the same chip are the same for all stars over the entire time range to within the errors. For example in F606W, the Amp A slope is -0.194% and the Amp B slope is -0.225%. Thus, we scale the amp B measurements to amp A, and the amp D measurements to amp C and then determine the rate of sensitivity change, using a linear fit. The scale factor represents the estimated flat-field error and is reported in Table 4. The results of the fits per individual amplifier are given in Tables 2 and 3, which list the filters, amplifier, number of observations, and the fitted slopes (percent change per year) and the associated errors. In Table 1 we list the average rate of sensitivity loss for each detector derived from a "refit" of each chip after scaling amps B and D to match amps A and C. All the filters show a decrease in sensitivity with time.

In Figure 2, we plot the average rate of loss per chip versus filter. The filters are color-coded by bandwidth: the broad-band filters are in red, medium-band filters in blue and long-pass filters in green. For chip 1 we see a relatively uniform λ-dependence (curved structure) to the sensitivity loss while with chip 2 we see the highest change in sensitivity at $\approx$ 5000-6000 Å.

The appendix contains the full set of plots of the temporal change in sensitivity for all stars and all filters used. These include the narrow-band (N), extremely wide (X), and long-pass (LP) filters, with the exception of F850LP).

Comparison to contamination monitor

We compared our photometry from the drizzled images (DRC files) to the contamination monitor results of Shanahan, Gosmeyer, and S. Baggett (2017). The latter used individual FLT images, after removing cosmic rays with the L.A.Cosmic program (van Dokkum, 2001), to measure aperture photometry. Figure 3 compares our results for GD153 to the contamination monitor results for F814W, as well as the FLC data. The overall observed-to-synthetic flux ratio is higher for the DRC (since CTE correction adds back lost flux) compared to the FLT. However, the decline in detector sensitivity is similar between the two monitoring programs though slightly steeper in the contam data possibly due to increasing CTE losses with time. The contamination monitor reports an average slope for each filter based on monte-carlo simulations of linear fits to the data. The FLC, as expected, shows increased scatter in the data but also shows the same overall decline in detector sensitivity.

Figure 5 shows the comparison between our drc results (average of the 4 calspec stars) with the contamination monitor flt results (for GRW+70 only, which has the most contam data and therefore the best temporal coverage) among the common filters. There is excellent agreement in both chips apart from the UV, where we find larger differences in sensitivity. Shanahan, Gosmeyer, and S. Baggett (2017) report almost no losses in sensitivity in the UV filters for GRW+70. In the ultraviolet, the change in sensitivity has an initial 3-year rise and then begins to decline, as shown in Figure 4, which is similar to what is seen in the STIS CCD (Bohlin, 2003). Thus for the UV filters (F218W, F225W, and F275W) we perform a linear fit to data obtained only after the 3rd year of WFC3 operation. The contamination monitor authors fit a linear regression to all the data points, leading to a flatter (and misleading)

Filter	Chip 1 Rate (%/yr)	Error	Total Num	Chip 2 Rate (%/yr)	Error	Total Num
F218W	-0.0841	0.0630	33	-0.1848	0.0534	33
F225W	-0.1932	0.0543	35	-0.2692	0.0474	33
F275W	-0.2111	0.0995	15	-0.1259	0.0309	19
F336W	-0.0482	0.0184	32	-0.0676	0.0546	24
F390M	-0.1697	0.1653	6	N/A	N/A	5
F390W	-0.1338	0.0533	17	N/A	N/A	4
F410M	-0.2001	0.0756	8	N/A	N/A	5
F438W	-0.1609	0.0140	54	-0.1563	0.0432	39
F467M	-0.2451	0.0521	9	-0.2949	0.0234	14
F475W	-0.2510	0.0309	27	-0.0927	0.0497	24
F547M	-0.2023	0.0254	22	-0.2030	0.0223	26
F555W	-0.2483	0.0238	31	-0.1282	0.0531	17
F606W	-0.2318	0.0143	44	-0.1744	0.0149	42
F621M	-0.2212	0.0230	21	-0.0637	0.0572	18
F625W	-0.2227	0.0404	21	-0.1742	0.0555	27
F689M	-0.1868	0.0656	8	N/A	N/A	4
F763M	-0.2042	0.0962	6	N/A	N/A	5
F775W	-0.1220	0.0363	21	-0.0988	0.0500	28
F814W	-0.1486	0.0180	41	-0.1383	0.0139	43
F845M	-0.1770	0.0303	19	-0.0618	0.0676	17
F850LP	-0.2306	0.0610	22	-0.1192	0.0811	9

Table 1: The rate of sensitivity loss in percent per year for Chip 1 and Chip 2 for all filters, where the percent change in sensitivity per year corresponds to 100 times the slope 'm' reported in the plots of sensitivity versus time. These values are the same as listed in the 'refit' columns of Tables 2 and 3 but are listed here for convenience and for easy comparison.

overall linear fit profile.

Recommendations

For improved photometric performance, we recommend temporal correction of UVIS data which can be performed manually as described below. The sensitivity losses reported in Tables 1 can be used to correct count rates for sources observed in UVIS chip 1 and chip 2, respectively, using the refit slope column values. The flux for observations taken at different epochs can be corrected by Equation 1 in order to improve relative photometry (instrumental magnitudes can be corrected via Equation 2). Note that the slope refers to the values (in percent) given in Table 1.

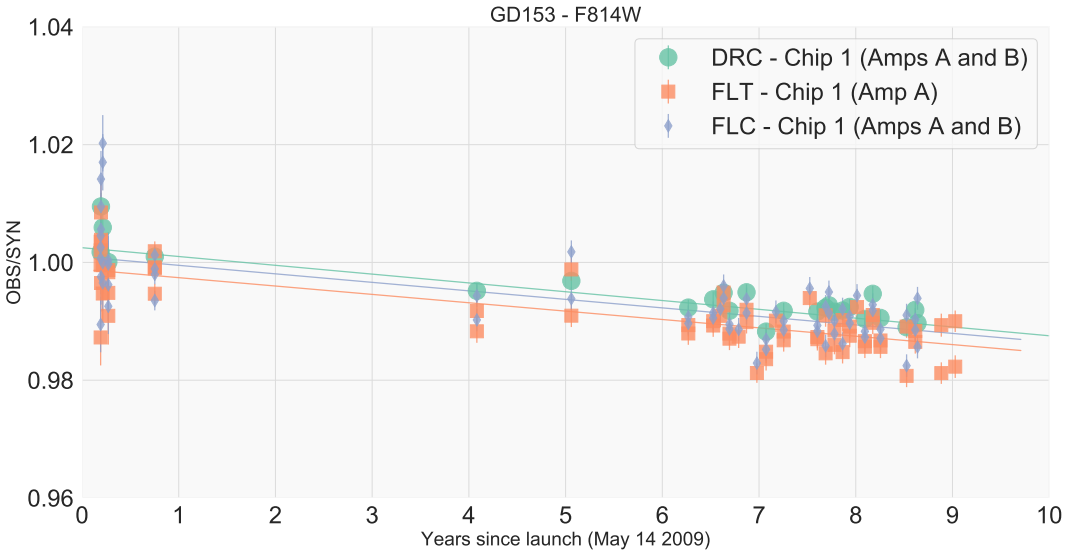

Figure 3: Comparison of the sensitivity loss rate for chip 1 between the observations in this project (DRC images) to the contamination monitor (FLT images) results and the FLC data in F814W for GD153 (the standard star in common between the two studies). For a plot of the DRC photometry for all 4 standards see Appendix Figure A19

$$Cr(t_2) < Cr(t_1), t_2 > t_1$$

$$\text{Flux}_{\text{corrected}}(t_2) = \text{PHOTFLAM} \times \left[Cr(t_2) \times \left(1 - \frac{\text{slope} \times (t_2 - t_1)}{100} \right) \right] \quad (1)$$

$$m_{corrected}(t_2) = m(t_2) - 2.5 \log \left(1 - \frac{\text{slope}\,(t_2 - t_1)}{100} \right) \quad (2)$$

$Cr(t_2)$ and $Cr(t_1)$ refer to the count-rate of the observation taken at epoch 2 and epoch 1 (respectively), where t_2 is an epoch corresponding to a date after t_1. It is expected that the count-rate for the later epoch data is lower than the count-rate for the epoch 1 data and so epoch 2 would be normalized to epoch 1 via this formula. PHOTFLAM refers to the inverse sensitivity value populated in the image header. For single epoch observations we do not recommend using this correction as the absolute flux calibration is still limited to the 1-2% level (Deustua et al., 2017). There are also additional sources of uncertainty regarding the correction that we list here.

1. The latest photometric calibration is based on the average of all observations obtained between 2009 and 2015, without applying any time-dependent or spatial-dependent corrections, and with all standard stars (GD-153, G191B2B, GD-71, P330E) weighted equally.

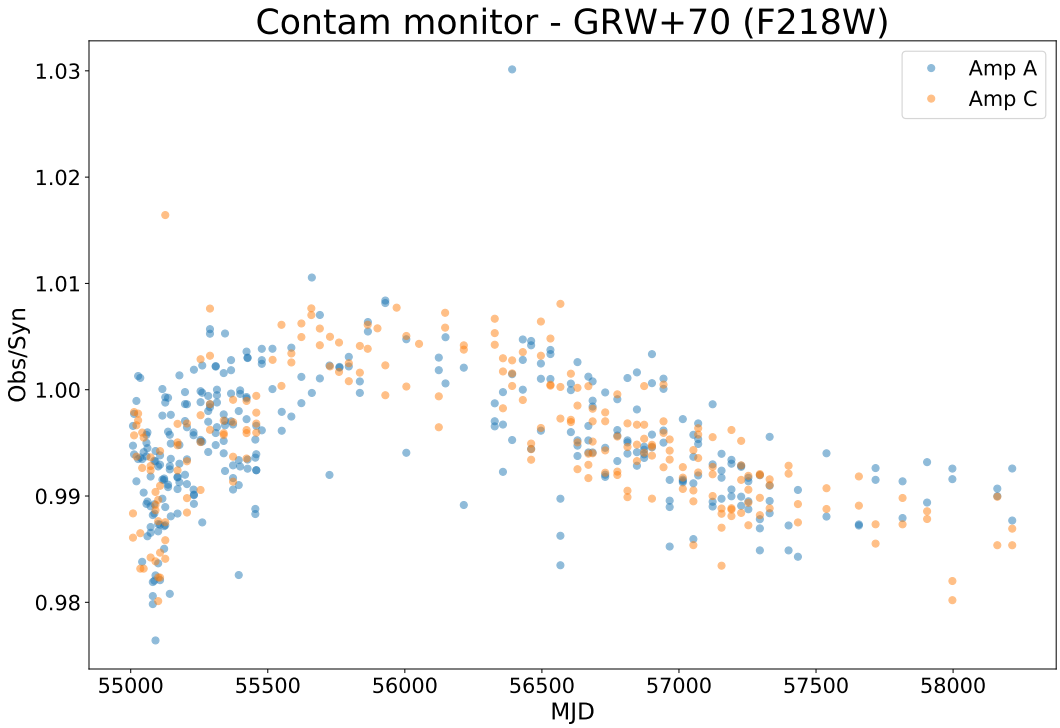

Figure 4: Observed-to-Synthetic photometry ratio for GRW+705824 (hereby GRW+70) in F218W from the contamination (contam) monitor described in Shanahan et al 2017

2. The photometry for some filters varies significantly by amplifier, implying that the flat fields have a $\approx 1\%$ or more systematic error in the corners of the detector, and these were not accounted for in the absolute calibration.

3. Slopes for the three UV filters are not valid for the first 3 years in-flight, when the sensitivity appeared to increase slightly, as seen from the contamination monitoring data of the white dwarf standard GRW+70 (see Figure 4).

Summary

In this report we compute temporal losses in the UVIS detectors sensitivity based on repeated observations of photometric standards. We compared aperture photometry of the stars to synthetic photometry and find losses from 0.1% to 0.3% per year for all filters. Contrary to the findings from the UVIS contamination monitor, we find non-zero losses in sensitivity for the UV filters up to 0.3% per year in both chips. Based on our findings in this report, we recommend temporal correction of UVIS data for improved photometric precision of relative photometry at different epochs. The absolute accuracy of the photometric calibration is still limited at the level of 1-2%. This study shows spatial variations in the detector sensitivity between different amplifiers, suggesting small errors in the flat field for some filters, typically

at a level ∼1%. For now, the sensitivity corrections may be applied manually to correct the photometry for multiple epochs. The WFC3 team is currently developing a time-dependent photometry reference file (IMPHTTAB) which will populate a unique inverse sensitivity (PHOTFLAM) value in the image header corresponding to the epoch of observation.

Acknowledgments

We thank Varun Bajaj for his assistance and advice on astrodrizzle and visit-level drizzling. We also greatly appreciate and thank Dr. Annalisa Calamida and Dr. Kailash Sahu for their detailed review of this report and their feedback.

References

Bajaj, V. and H. Khandrika (2017). "Comparing Aperture Photometry Software Packages". In: *Space Telescope WFC3 Instrument Science Report 2017-10*.

Bohlin, R. C. (2003). "STIS Flux Calibration". In: *HST Calibration Workshop : Hubble after the Installation of the ACS and the NICMOS Cooling System*.

Deustua, S. E. et al. (2017). "WFC3/UVIS Updated 2017 Chip-Dependent Inverse Sensitivity Values". In:

Hilbert, B. (2009). "WFC3 SMOV Program 11427: UVIS Channel Shutter Shading". In: *Instrument Science Report WFC3 2009-25, 22 pages*.

Mack, J., A. Rajan, and A. Bowers (2015). *Spatial Accuracy of the UVIS Flat Fields*. Tech. rep.

Ryan R. E., Jr. et al. (2016). "The Updated Calibration Pipeline for WFC3/UVIS: a Reference Guide to calwf3 (version 3.3)". In: *Space Telescope WFC3 Instrument Science Report 2016-01*.

Sabbi, E. and A. Bellini (2013). "UVIS PSF Spatial & Temporal Variations". In: *Instrument Science Report WFC3 2013-11, 10 pages*.

Sahu, Kailash, C. M. Gosmeyer, and Sylvia Baggett (2015). "WFC3/UVIS Shutter Characterization". In: *Instrument Science Report WFC3 2015-12, 11 pages*.

Shanahan, C. E., C. M. Gosmeyer, and S. Baggett (2017). "2017 Update on the WFC3/UVIS Stability and Contamination Monitor". In: *Space Telescope WFC3 Instrument Science Report 2017-15*.

Stetson, P. B. (1987). "DAOPHOT - A computer program for crowded-field stellar photometry". In: *Publications of the Astronomical Society of the Pacific* 99, pp. 191–222. DOI: 10.1086/131977.

Tokunaga, A. T. and W. D. Vacca (2005). "The Mauna Kea Observatories Near-Infrared Filter Set. III. Isophotal Wavelengths and Absolute Calibration". In: *Publications of the Astronomical Society of the Pacific* 117, pp. 421–426. DOI: 10.1086/429382. eprint: astro-ph/0502120.

van Dokkum, Pieter G. (2001). "Cosmic-Ray Rejection by Laplacian Edge Detection". In: *Publications of the Astronomical Society of the Pacific* 113. DOI: 10.1086/323894. arXiv: astro-ph/0108003 [astro-ph].

Filter	Amp 1	Slope (%) ± Error	Num	Amp 2	Slope (%) ± Error	Num	Refit slope (%) ± Error
F218W	A	-0.1734 ± 0.0652	29	B	0.0019 ± 0.2119	10	-0.0841 ± 0.0630
F225W	A	-0.1040 ± 0.0594	43	B	0.0191 ± 0.1446	10	-0.1932 ± 0.0543
F275W	A	-0.1120 ± 0.1987	24	B	-0.1593 ± 0.1315	12	-0.2111 ± 0.0995
F336W	A	-0.0407 ± 0.0349	22	B	-0.0474 ± 0.0537	12	-0.0482 ± 0.0184
F390M	A	N/A ± N/A	4	B	N/A ± N/A	2	-0.1697 ± 0.1653
F390W	A	-0.1333 ± 0.0847	15	B	N/A ± N/A	2	-0.1338 ± 0.0533
F410M	A	-0.1927 ± 0.0594	6	B	N/A ± N/A	2	-0.2001 ± 0.0756
F438W	A	-0.1612 ± 0.0150	43	B	-0.1633 ± 0.0938	12	-0.1609 ± 0.0140
F467M	A	-0.3508 ± 0.1638	8	B	N/A ± N/A	2	-0.2451 ± 0.0521
F475W	A	-0.2557 ± 0.0605	15	B	-0.1558 ± 0.1278	12	-0.2510 ± 0.0309
F547M	A	-0.2058 ± 0.0398	10	B	-0.1816 ± 0.0926	12	-0.2023 ± 0.0254
F555W	A	-0.1747 ± 0.0441	19	B	-0.1162 ± 0.1477	12	-0.2483 ± 0.0238
F606W	A	-0.1939 ± 0.0194	33	B	-0.2247 ± 0.0652	12	-0.2318 ± 0.0143
F621M	A	-0.2272 ± 0.0401	9	B	-0.1777 ± 0.0700	12	-0.2212 ± 0.0230
F625W	A	-0.2345 ± 0.0805	9	B	-0.0785 ± 0.0795	12	-0.2227 ± 0.0404
F689M	A	-0.1915 ± 0.0977	6	B	N/A ± N/A	2	-0.1868 ± 0.0656
F763M	A	N/A ± N/A	4	B	N/A ± N/A	2	-0.2042 ± 0.0962
F775W	A	-0.1787 ± 0.0819	11	B	-0.1073 ± 0.1030	12	-0.1220 ± 0.0363
F814W	A	-0.0591 ± 0.0225	29	B	-0.1234 ± 0.0745	12	-0.1486 ± 0.0180
F845M	A	-0.1856 ± 0.0592	8	B	-0.1132 ± 0.0772	11	-0.1770 ± 0.0303
F850LP	A	-0.2410 ± 0.0981	18	B	-0.1224 ± 0.1995	4	-0.2306 ± 0.0610

Table 2: The slopes of the individual amps' data (for Chip 1) with the slope of the final refit data with the amp offsets (see Table 4) applied in order to correct for any spatial variations due to flat fielding errors. N/A values are listed for filters/amps with less than 6 observations. While some amp B slope values are positive due to large uncertainty (due to few points), the overall trend is consistent with amp A.

Filter	Amp 1	Slope (%) ± Error	Num	Amp 2	Slope (%) ± Error	Num	Refit slope (%) ± Error
F218W	C	-0.0993 ± 0.0703	29	D	0.0769 ± 0.5236	7	-0.1848 ± 0.0534
F225W	C	-0.2618 ± 0.0551	30	D	0.0881 ± 0.3087	7	-0.2692 ± 0.0474
F275W	C	-0.1388 ± 0.0552	20	D	-0.1485 ± 0.0528	8	-0.1259 ± 0.0309
F336W	C	-0.1801 ± 0.0744	19	D	0.0272 ± 0.0970	8	-0.0676 ± 0.0546
F390M	C	N/A ± N/A	3	D	N/A ± N/A	2	N/A ± N/A
F390W	C	N/A ± N/A	2	D	N/A ± N/A	2	N/A ± N/A
F410M	C	N/A ± N/A	3	D	N/A ± N/A	2	N/A ± N/A
F438W	C	-0.1557 ± 0.0514	31	D	-0.1565 ± 0.1293	8	-0.1563 ± 0.0432
F467M	C	-0.2947 ± 0.0269	12	D	N/A ± N/A	2	-0.2949 ± 0.0234
F475W	C	-0.1070 ± 0.0814	18	D	-0.0824 ± 0.0923	8	-0.0927 ± 0.0497
F547M	C	-0.2167 ± 0.0209	19	D	-0.0594 ± 0.0962	8	-0.2030 ± 0.0223
F555W	C	-0.1957 ± 0.1021	9	D	-0.0345 ± 0.0583	8	-0.1282 ± 0.0531
F606W	C	-0.1165 ± 0.0375	35	D	-0.2022 ± 0.0681	8	-0.1744 ± 0.0149
F621M	C	-0.0767 ± 0.1018	10	D	-0.0566 ± 0.0957	8	-0.0637 ± 0.0572
F625W	C	-0.1818 ± 0.0758	19	D	-0.1132 ± 0.1129	8	-0.1742 ± 0.0555
F689M	C	N/A ± N/A	3	D	N/A ± N/A	1	N/A ± N/A
F763M	C	N/A ± N/A	3	D	N/A ± N/A	2	N/A ± N/A
F775W	C	-0.1298 ± 0.0571	20	D	-0.0032 ± 0.0761	8	-0.0988 ± 0.0500
F814W	C	-0.1375 ± 0.0126	36	D	-0.0320 ± 0.0902	8	-0.1383 ± 0.0139
F845M	C	-0.0735 ± 0.1370	10	D	-0.0543 ± 0.0925	7	-0.0618 ± 0.0676
F850LP	C	-0.0904 ± 0.1020	6	D	N/A ± N/A	3	-0.1192 ± 0.0811

Table 3: Same as Table 2 but for Chip 2

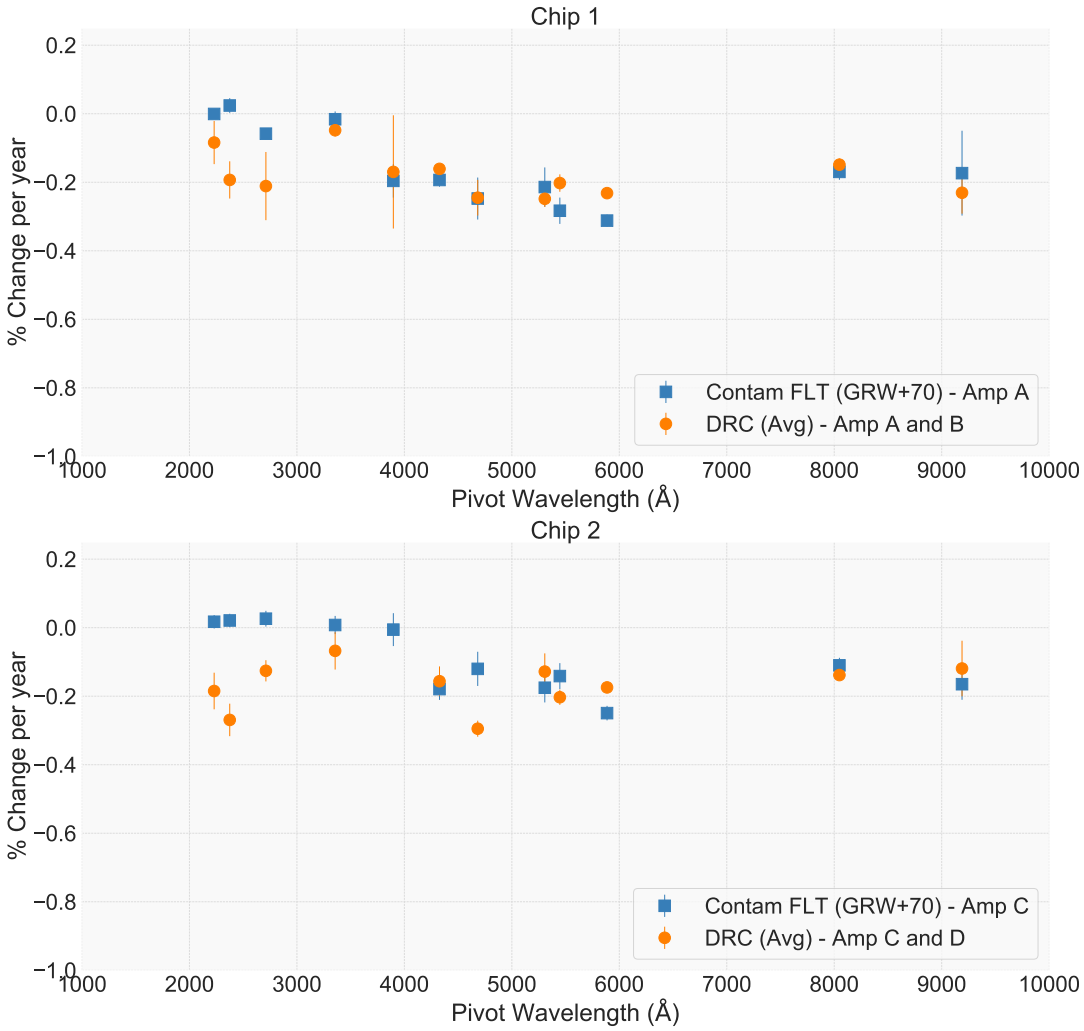

Figure 5: Change in sensitivity derived from FLT observations of GRW+70 from the UVIS contamination monitor (blue squares) and from an average of DRC photometry for all the stars in our study (orange circles). Differences for the 3 bluest filters are due to different fit techniques, where the DRC fits exclude data at t $<$ 3 years, when the sensitivity was increasing.

Filter	Amp B/A offset	Amp D/C offset
F218W	+0.583%	+2.359%
F225W	-0.560%	+0.250%
F275W	-0.258%	-1.030%
F336W	-0.010%	+0.060%
F390M	-0.590%	N/A
F390W	-0.920%	N/A
F410M	-0.583%	N/A
F438W	-0.730%	-0.670%
F467M	-0.620%	-0.710%
F475W	-0.641%	-0.968%
F547M	-0.967%	-0.996%
F555W	-0.973%	-0.860%
F606W	-1.388%	-1.070%
F621M	-0.710%	-0.640%
F625W	-0.706%	-0.716%
F689M	-1.218%	N/A
F763M	-0.624%	N/A
F775W	-0.330%	-0.100%
F814W	+0.182%	+0.127%
F845M	+1.118%	+0.154%
F850LP	-0.692%	+0.575%

Table 4: Offsets between Amp B vs A and Amp D vs C linear fits. Offsets are computed as $100 \times \left(\frac{B-A}{A}\right)$ and $100 \times \left(\frac{D-C}{C}\right)$ where A, B, C, and D represent the photometric values (Observed-to-Synthetic) for the respective amplifiers. Filters with N/A values had less than 6 observations and therefore a reliable fit could not be computed. Positive offset values represent an amp (B or D) that had higher values than the fiducial amp (A or C) and had to be scaled down to match, while negative offset values represent amps that had lower values than fiducial amps and had to be scaled up to match.

Appendix

Table A1: List of Proposal IDs for WFC3 photometry of the 4 HST standards used for absolute calibration of the UVIS detector

Proposal ID	Stars	Num images
11427	GD153	2
11450	GD153	60
11798	GD153	4
11903	GD153, G191B2B, P330E, GD71	89, 75, 46, 16
13089	GD153, P330E	76, 75
13575	GD153, P330E	76, 84
13711	GD153, G191B2B, GD71	15, 15, 15
14018	G191B2B	38
14019	GD153	1
14021	GD153, G191B2B, P330E	30, 30, 30
14382	GD153	99
14384	GD153, G191B2B, P330E, GD71	30, 30, 30, 32
14815	GD153	99
14883	GD153, G191B2B, P330E, GD71	30, 30, 30, 32
14992	GD153, GD71	30, 30

Table A2: Observation list for GD71

Filter	Date Range Chip 1	Num Obs Chip 1	Date Range Chip 2	Num Obs Chip 2
F218W	2016.627 - 2017.704	3	2016.656 - 2017.704	3
F225W	2010.613 - 2017.704	4	2016.656 - 2017.704	3
F275W	2010.613 - 2017.704	4	2014.686 - 2017.704	6
F336W	2010.613 - 2017.704	4	2014.686 - 2017.704	6
F350LP	2010.613 - 2017.613	3	2016.656 - 2017.616	2
F390W	2010.613 - 2010.613	1	N/A - N/A	0
F438W	2010.613 - 2017.704	4	2016.656 - 2017.704	3
F467M	N/A - N/A	0	2010.613 - 2010.613	1
F469N	N/A - N/A	0	2010.613 - 2010.613	1
F475W	2010.613 - 2017.704	4	2014.686 - 2017.704	6
F502N	N/A - N/A	0	2010.613 - 2010.613	1
F547M	2016.627 - 2017.704	3	2010.613 - 2017.704	4
F555W	2010.613 - 2017.704	4	2016.656 - 2017.704	3
F600LP	2016.627 - 2017.613	2	2016.656 - 2017.616	2
F606W	2016.627 - 2017.704	3	2010.613 - 2017.704	4
F621M	2016.627 - 2017.704	3	2016.656 - 2017.704	3
F625W	2016.627 - 2017.704	3	2014.686 - 2017.704	6
F657N	2017.704 - 2017.704	1	2017.704 - 2017.704	1
F775W	2010.613 - 2017.704	4	2014.686 - 2017.704	6
F814W	2016.627 - 2017.704	3	2010.613 - 2017.704	4
F845M	2016.627 - 2017.613	2	2016.656 - 2017.616	2
F850LP	2010.613 - 2010.613	1	N/A - N/A	0
F953N	2017.704 - 2017.704	1	2017.704 - 2017.704	1

Table A3: Observation list for G191B2B

Filter	Date Range Chip 1	Num Obs Chip 1	Date Range Chip 2	Num Obs Chip 2
F218W	2015.115 - 2017.249	4	2015.116 - 2017.246	4
F225W	2009.858 - 2017.249	8	2015.116 - 2017.246	5
F275W	2009.858 - 2017.249	7	2014.917 - 2017.246	7
F280N	2009.769 - 2009.769	1	2009.770 - 2009.770	1
F336W	2009.858 - 2017.249	7	2014.917 - 2017.246	7
F373N	2009.769 - 2009.769	1	2009.770 - 2009.770	1
F390M	2015.115 - 2015.115	1	2015.116 - 2015.116	1
F395N	2009.769 - 2009.769	1	2009.770 - 2009.770	1
F410M	2015.115 - 2015.115	1	2015.116 - 2015.116	1
F438W	2009.858 - 2017.249	7	2015.116 - 2017.246	4
F467M	2009.769 - 2015.115	2	2009.858 - 2015.116	4
F469N	2009.769 - 2009.769	1	2009.740 - 2010.606	6
F475W	2015.627 - 2017.249	3	2014.917 - 2017.246	6
F487N	2009.769 - 2009.769	1	2009.770 - 2009.770	1
F502N	2009.769 - 2009.769	1	2009.740 - 2010.606	6
F547M	2015.115 - 2017.249	4	2009.858 - 2017.246	7
F555W	2015.627 - 2017.249	3	2015.615 - 2017.246	3
F600LP	2015.115 - 2017.249	4	2015.116 - 2017.246	4
F606W	2015.627 - 2017.249	3	2015.615 - 2017.246	3
F621M	2015.115 - 2017.249	4	2015.116 - 2017.246	4
F625W	2015.115 - 2017.249	4	2014.917 - 2017.246	7
F631N	2009.769 - 2009.769	1	2009.770 - 2009.770	1
F645N	2009.769 - 2009.769	1	2009.770 - 2009.770	1
F656N	2009.769 - 2009.769	1	2009.770 - 2009.770	1
F657N	2009.769 - 2009.769	1	2009.770 - 2009.770	1
F658N	2009.769 - 2009.769	1	2009.769 - 2009.769	1
F665N	2009.769 - 2009.769	1	2009.769 - 2009.769	1
F673N	2009.769 - 2009.769	1	2009.769 - 2009.769	1
F680N	2009.769 - 2009.769	1	2009.769 - 2009.769	1
F689M	2015.115 - 2015.115	1	2015.116 - 2015.116	1
F763M	2015.115 - 2015.115	1	2015.116 - 2015.116	1
F775W	2009.769 - 2017.249	5	2009.770 - 2017.246	8
F814W	2009.769 - 2017.249	5	2009.740 - 2017.246	10
F845M	2009.769 - 2017.249	5	2015.116 - 2017.246	4
F850LP	2009.739 - 2015.115	6	2009.770 - 2015.116	2
F953N	2009.769 - 2009.769	1	2009.769 - 2009.769	1

Table A4: Observation list for GD153

Filter	Date Range Chip 1	Num Obs Chip 1	Date Range Chip 2	Num Obs Chip 2
F218W	2009.529 - 2017.975	28	2013.035 - 2017.952	27
F225W	2009.529 - 2017.975	37	2013.035 - 2017.952	27
F275W	2009.529 - 2017.975	18	2013.035 - 2017.862	10
F280N	2009.529 - 2014.408	3	2013.026 - 2014.425	2
F300X	2009.529 - 2009.529	1	N/A - N/A	0
F336W	2009.529 - 2017.975	16	2013.035 - 2017.862	9
F343N	2009.529 - 2014.396	3	2013.174 - 2014.458	2
F350LP	2009.927 - 2010.565	5	N/A - N/A	0
F373N	2009.529 - 2014.396	3	2013.174 - 2014.458	2
F390M	2009.529 - 2014.396	3	2013.038 - 2014.458	2
F390W	2009.529 - 2014.390	12	2013.035 - 2013.922	2
F395N	2009.529 - 2014.396	4	2009.533 - 2014.874	4
F410M	2009.529 - 2014.396	3	2013.026 - 2014.458	2
F438W	2009.529 - 2017.975	37	2013.035 - 2017.952	27
F467M	2009.529 - 2014.396	4	2009.874 - 2014.458	7
F469N	2009.529 - 2014.408	4	2009.874 - 2014.425	7
F475W	2009.529 - 2017.975	13	2013.026 - 2017.862	9
F475X	2009.529 - 2009.529	1	N/A - N/A	0
F487N	2009.529 - 2014.408	3	2013.174 - 2014.425	2
F502N	2009.529 - 2014.408	4	2009.874 - 2014.425	7
F547M	2009.529 - 2017.975	8	2009.874 - 2017.862	11
F555W	2009.529 - 2017.975	17	2013.026 - 2017.862	6
F600LP	2009.529 - 2017.059	6	2013.035 - 2017.020	5
F606W	2009.529 - 2017.975	32	2009.874 - 2017.952	31
F621M	2009.529 - 2017.975	7	2013.026 - 2017.862	6
F625W	2009.529 - 2017.975	7	2013.038 - 2017.862	9
F631N	2013.400 - 2014.408	2	2013.174 - 2014.425	2
F645N	2009.529 - 2014.408	4	2013.174 - 2014.425	2
F656N	2009.529 - 2014.408	3	2013.174 - 2014.425	2
F657N	2013.400 - 2017.975	3	2013.174 - 2017.862	3
F658N	2009.530 - 2014.396	3	2013.038 - 2014.458	2
F665N	2009.530 - 2014.408	3	2013.174 - 2014.425	2
F673N	2009.530 - 2014.408	3	2013.174 - 2014.425	2
F680N	2013.400 - 2014.408	2	2013.174 - 2014.425	2
F689M	2009.530 - 2014.396	4	2013.026 - 2014.458	2
F763M	2009.530 - 2014.396	3	2013.026 - 2014.458	2
F775W	2009.529 - 2017.975	7	2013.038 - 2017.862	9
F814W	2009.529 - 2017.975	26	2009.874 - 2017.952	25
F845M	2009.530 - 2017.975	7	2013.026 - 2017.862	6
F850LP	2009.874 - 2014.390	8	2013.035 - 2013.922	2
F953N	2009.530 - 2014.408	3	2013.026 - 2014.425	2

Table A5: Observation list for P330E

Filter	Date Range Chip 1	Num Obs Chip 1	Date Range Chip 2	Num Obs Chip 2
F200LP	2009.953 - 2014.071	4	2013.097 - 2014.345	2
F218W	2009.953 - 2014.071	4	2013.153 - 2014.345	2
F225W	2009.953 - 2014.071	4	2013.153 - 2014.345	2
F275W	2009.953 - 2017.426	7	2013.153 - 2017.439	5
F280N	2014.071 - 2014.071	1	2014.390 - 2014.390	1
F300X	2009.953 - 2014.051	4	2013.153 - 2014.345	2
F336W	2009.953 - 2017.426	7	2013.153 - 2017.439	5
F343N	2013.551 - 2014.071	2	2013.153 - 2014.390	2
F350LP	2009.953 - 2017.426	7	2013.097 - 2017.439	5
F373N	2013.298 - 2014.071	2	2013.035 - 2014.390	2
F390M	2013.551 - 2014.071	2	2013.153 - 2014.345	2
F390W	2009.953 - 2013.898	4	2013.097 - 2014.358	2
F395N	2014.071 - 2014.071	1	2013.035 - 2014.390	2
F410M	2009.953 - 2013.898	4	2013.097 - 2014.358	2
F438W	2009.953 - 2017.426	7	2013.097 - 2017.439	5
F467M	2009.953 - 2013.898	4	2013.097 - 2014.358	2
F469N	2013.298 - 2014.071	2	2013.035 - 2014.391	2
F475W	2009.953 - 2017.426	7	2013.153 - 2017.439	5
F475X	2009.953 - 2014.051	4	2013.153 - 2014.345	2
F487N	2013.298 - 2014.071	2	2013.035 - 2014.391	2
F502N	2013.298 - 2014.071	2	2013.035 - 2014.391	2
F547M	2009.953 - 2017.426	7	2013.153 - 2017.439	5
F555W	2009.953 - 2017.426	7	2013.153 - 2017.439	5
F600LP	2009.953 - 2017.426	7	2013.153 - 2017.439	5
F606W	2009.953 - 2017.426	7	2013.097 - 2017.439	5
F621M	2009.953 - 2017.426	7	2013.097 - 2017.439	5
F625W	2009.953 - 2017.426	7	2013.097 - 2017.439	5
F631N	2014.071 - 2014.071	1	2014.391 - 2014.391	1
F645N	2013.298 - 2014.071	2	2013.035 - 2014.391	2
F656N	2013.298 - 2014.071	2	2013.035 - 2014.391	2
F657N	2013.298 - 2014.051	2	2013.035 - 2014.345	2
F658N	2013.108 - 2013.898	2	2013.097 - 2014.358	2
F665N	2013.298 - 2014.051	2	2013.035 - 2014.345	2
F673N	2013.298 - 2014.051	2	2013.035 - 2014.345	2
F680N	2013.898 - 2013.898	1	2014.358 - 2014.358	1
F689M	2009.953 - 2013.898	3	2014.358 - 2014.358	1
F763M	2013.108 - 2013.898	2	2013.097 - 2014.358	2
F775W	2009.953 - 2017.426	7	2013.097 - 2017.439	5
F814W	2009.953 - 2017.426	7	2013.097 - 2017.439	5
F845M	2013.108 - 2017.426	5	2013.097 - 2017.439	5
F850LP	2009.953 - 2017.426	7	2013.153 - 2017.439	5
F953N	2013.108 - 2013.898	2	2013.097 - 2014.358	2

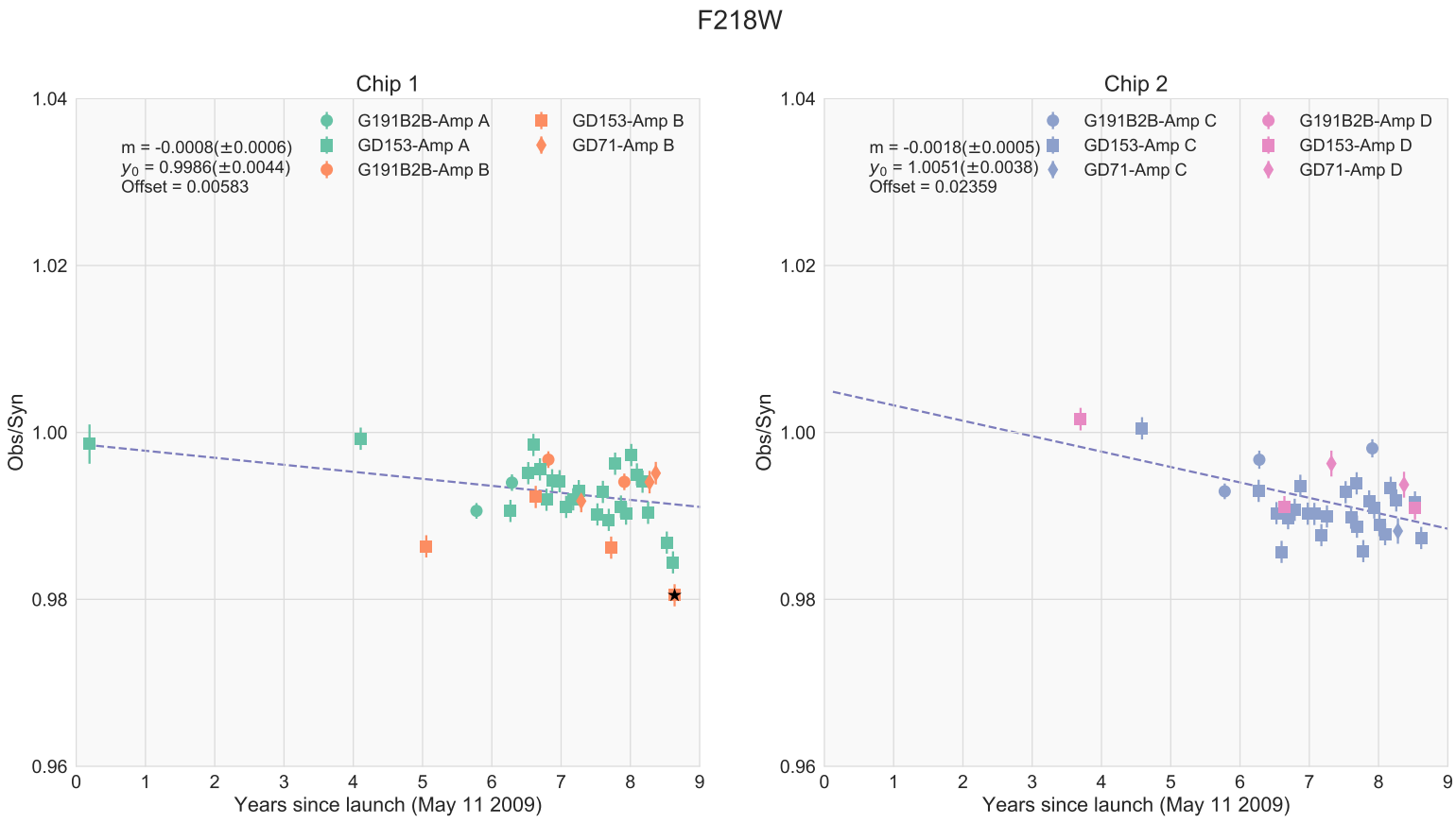

Figure A1: The observed-to-synthetic photometry ratio versus time of observation in years (since launch date) for all stars in F218W, separated by Chip 1 and Chip 2 data. A linear fit to the results is overplotted with the slopes, y-intercepts and associated errors given in the figure legend. As described in the text, amps B and D have been scaled by a constant to correct for any residual flat-field errors in the corners of the detector, indicated by 'offset' in the figure legend. For three UV filters, the fits are only for t $>$ 3 years. Positive value means amp B (or amp D) had higher values than amp A (or C). Black stars indicate points rejected from the linear fits via sigma-clipping. Therefore the slope is the 'refit' combined fit.

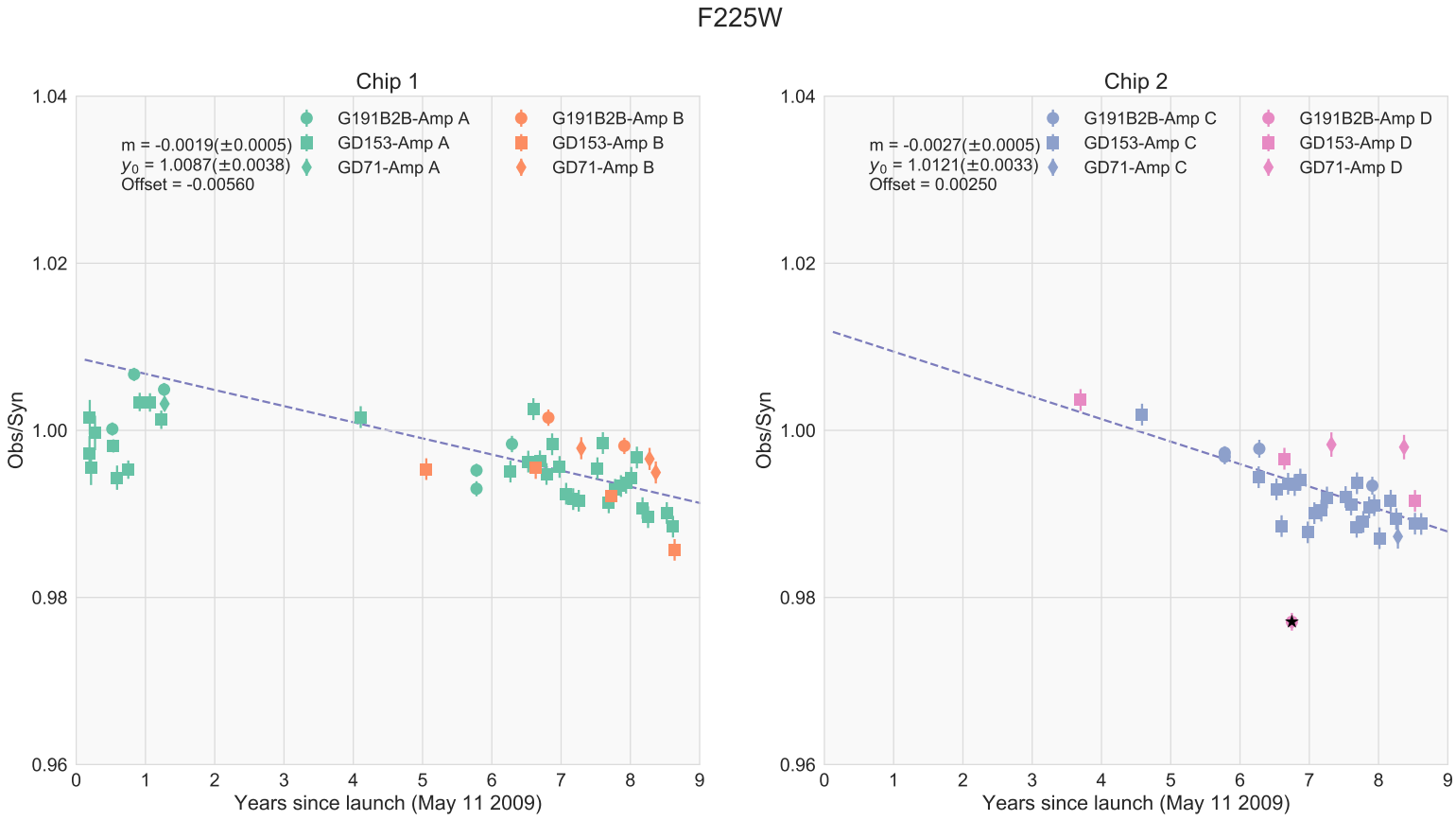

Figure A2: Same as Figure A1 but for F225W for t > 3 years.

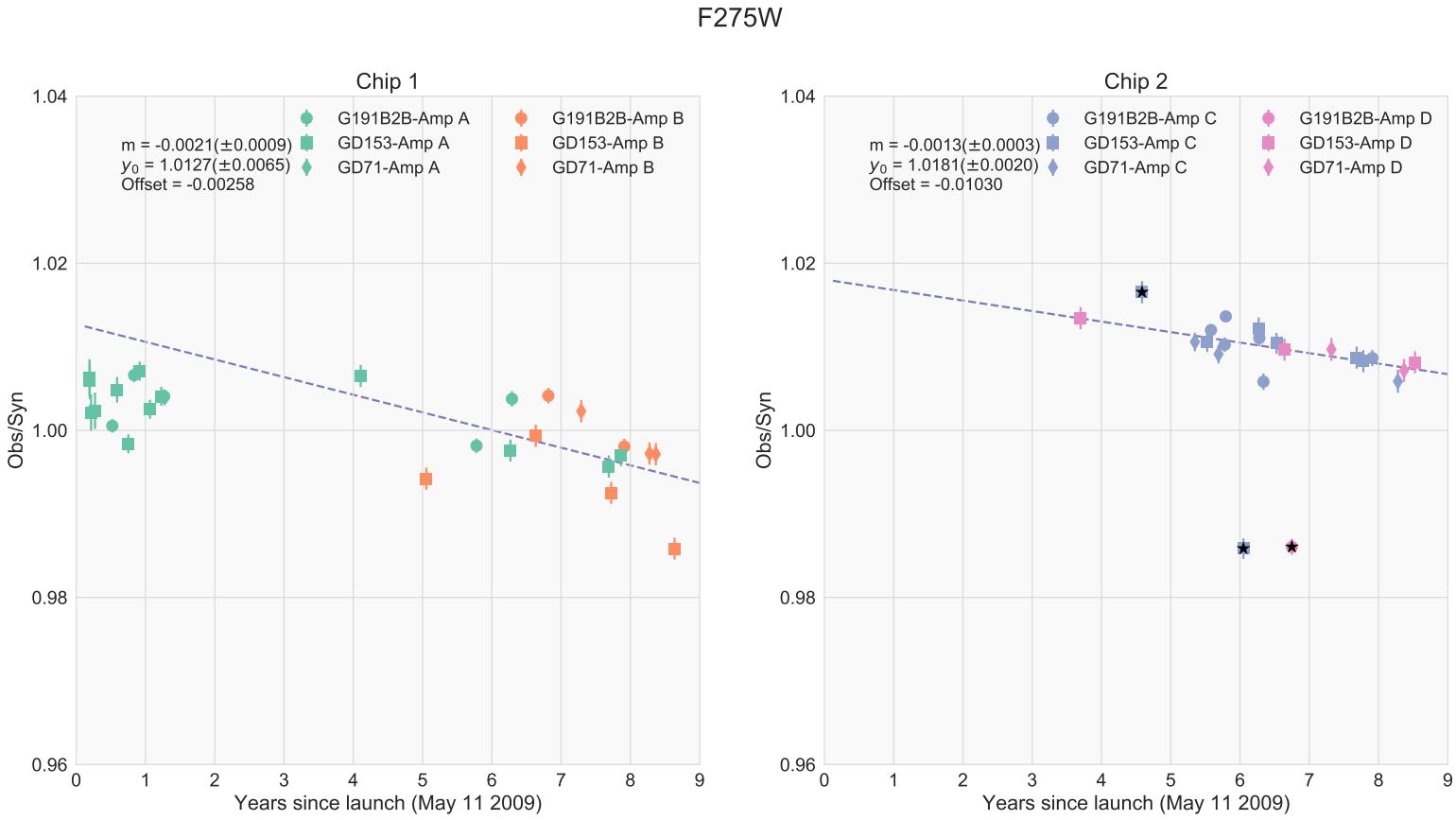

Figure A3: Same as Figure A1 but for F275W for t > 3 years.

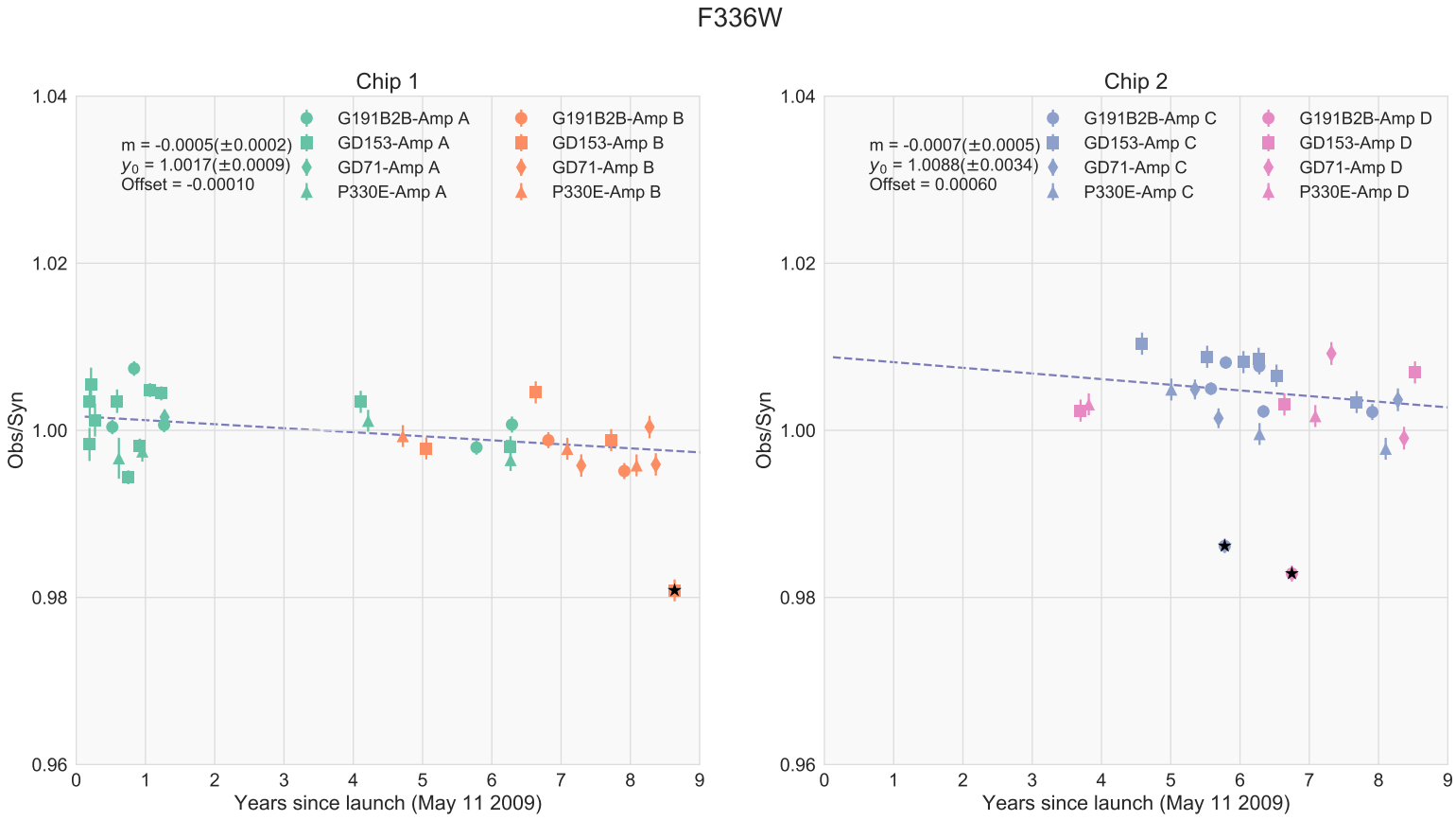

Figure A4: Same as Figure A1 but for F336W

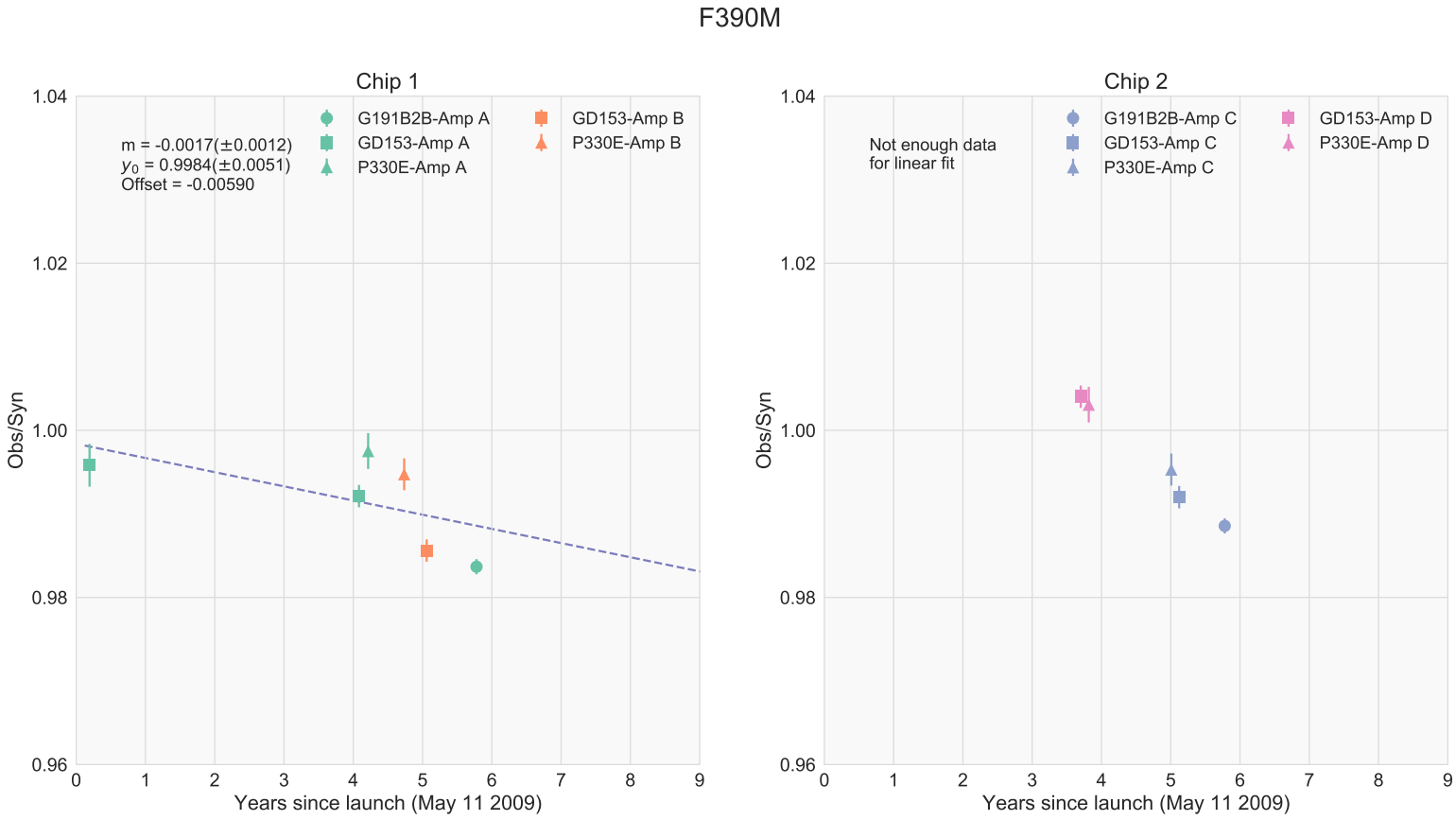

Figure A5: Same as Figure A1 but for F390M

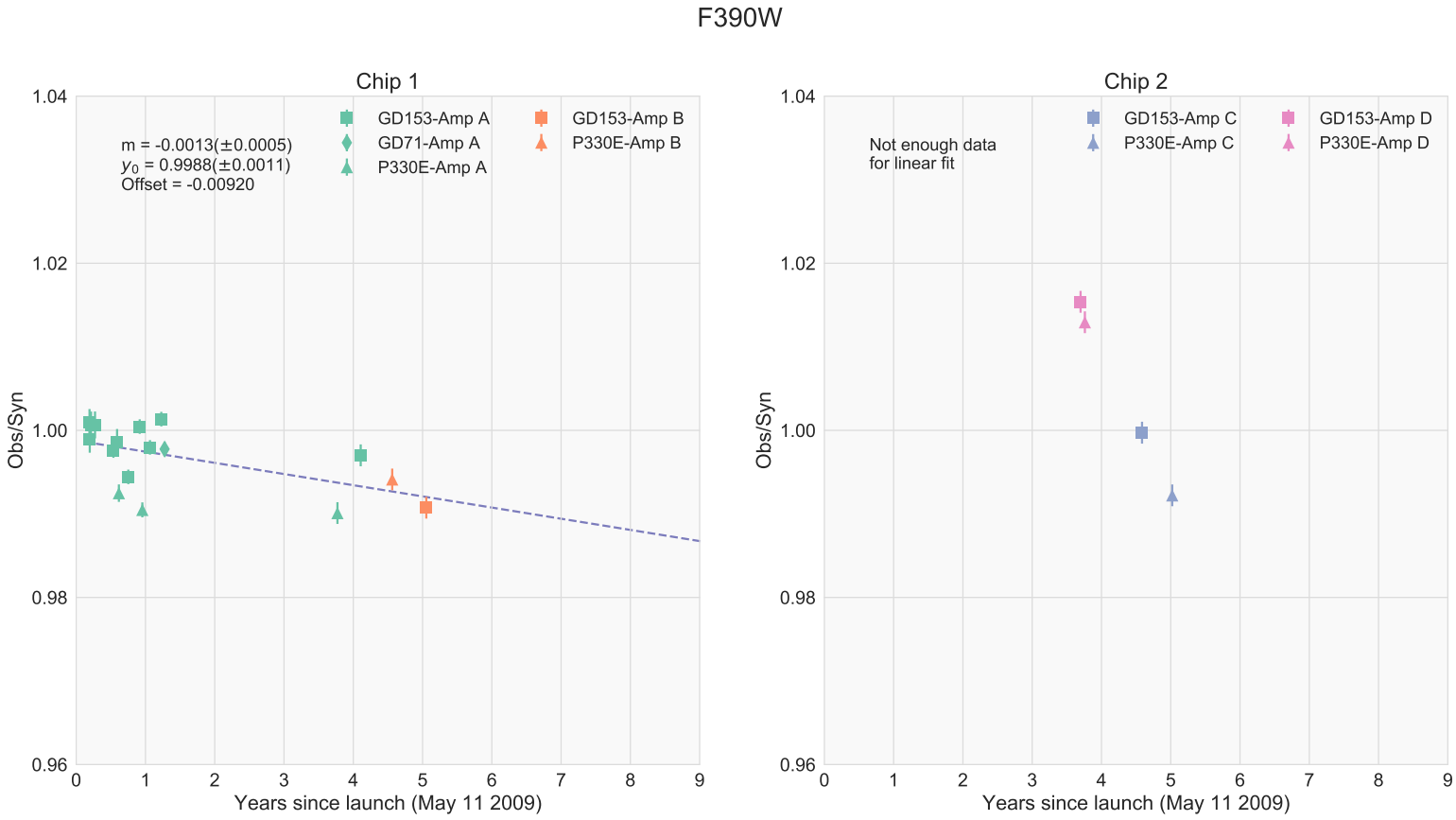

Figure A6: Same as Figure A1 but for F390W

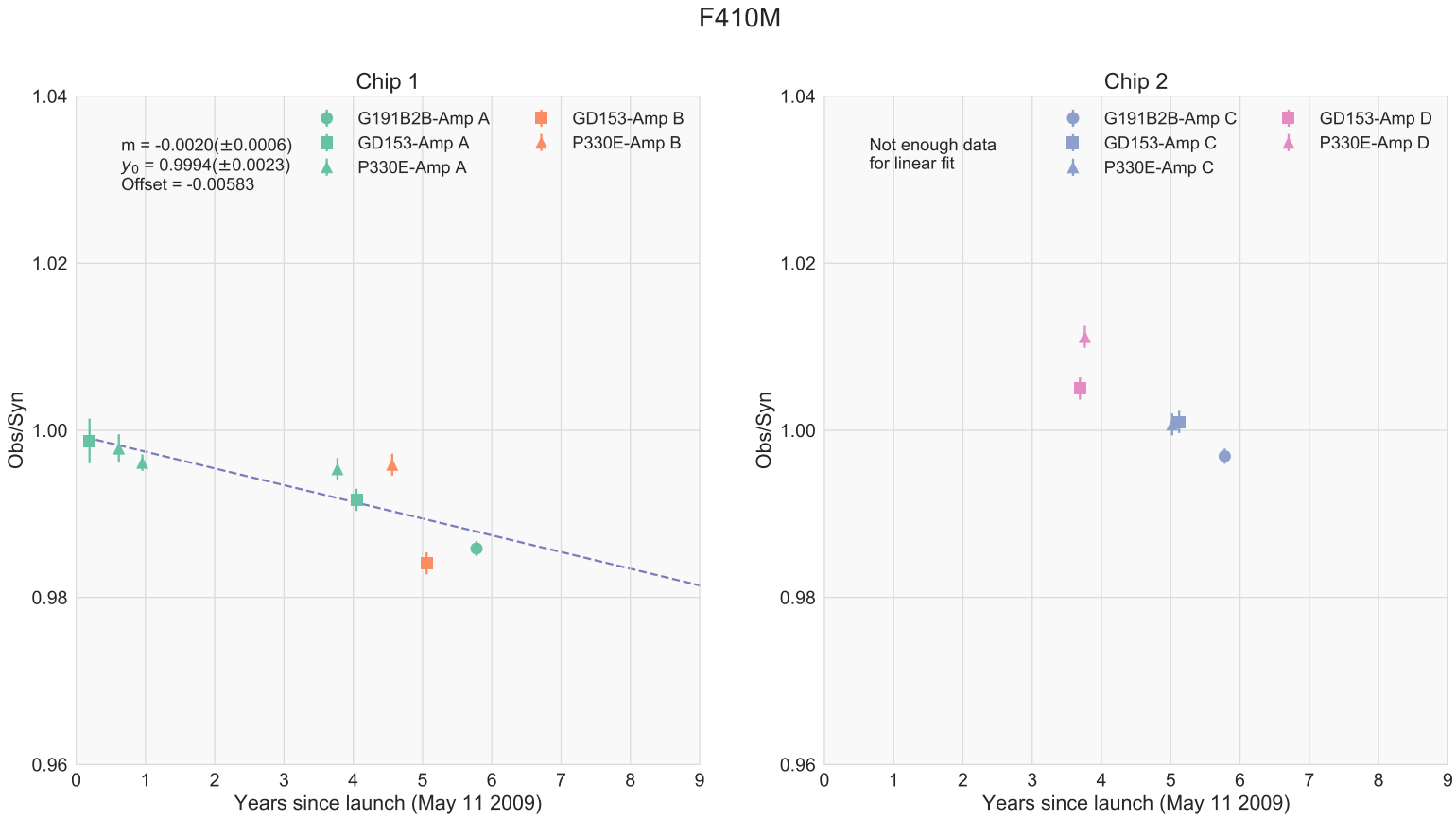

Figure A7: Same as Figure A1 but for F410M

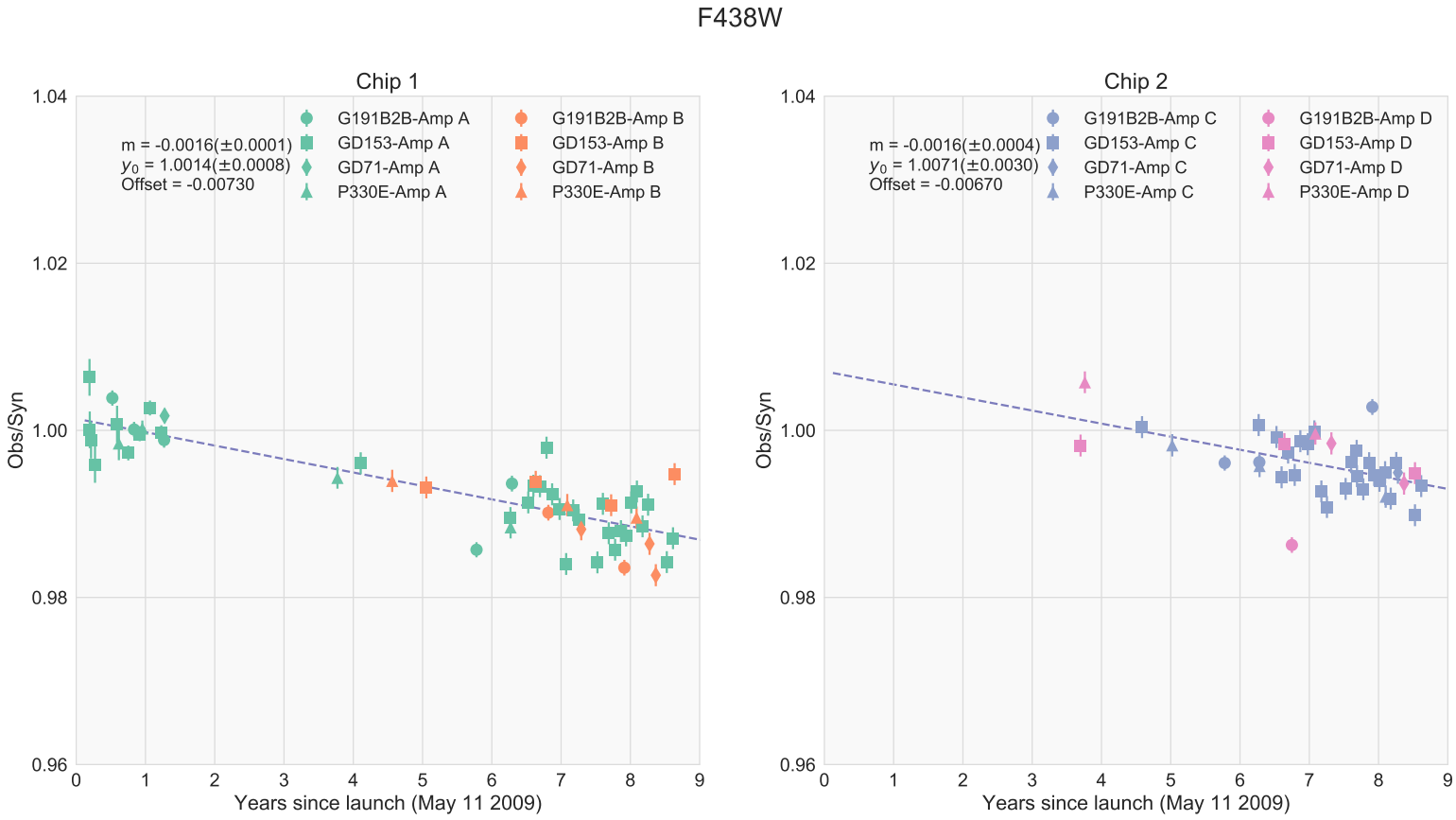

Figure A8: Same as Figure A1 but for F438W

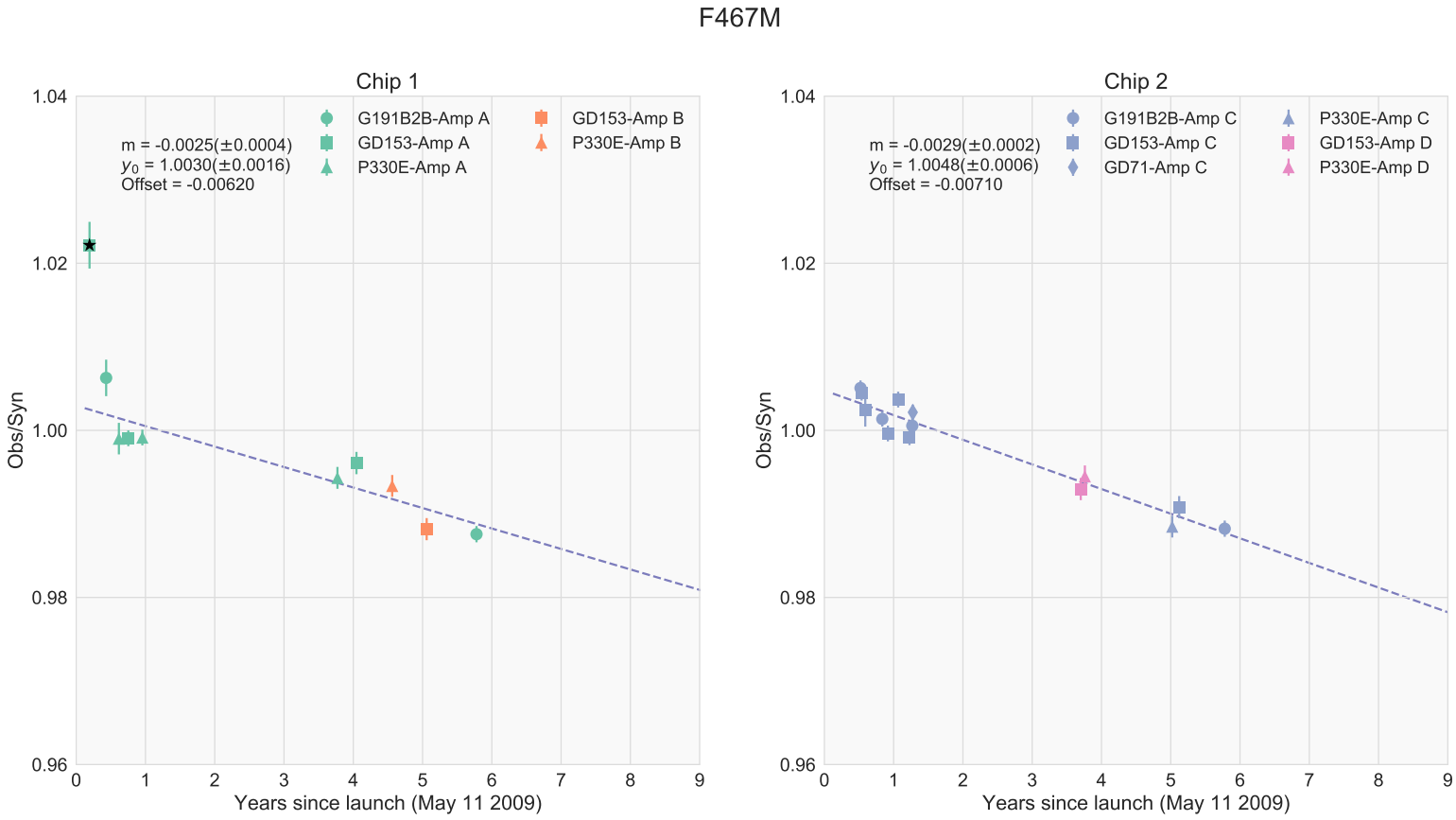

Figure A9: Same as Figure A1 but for F467M

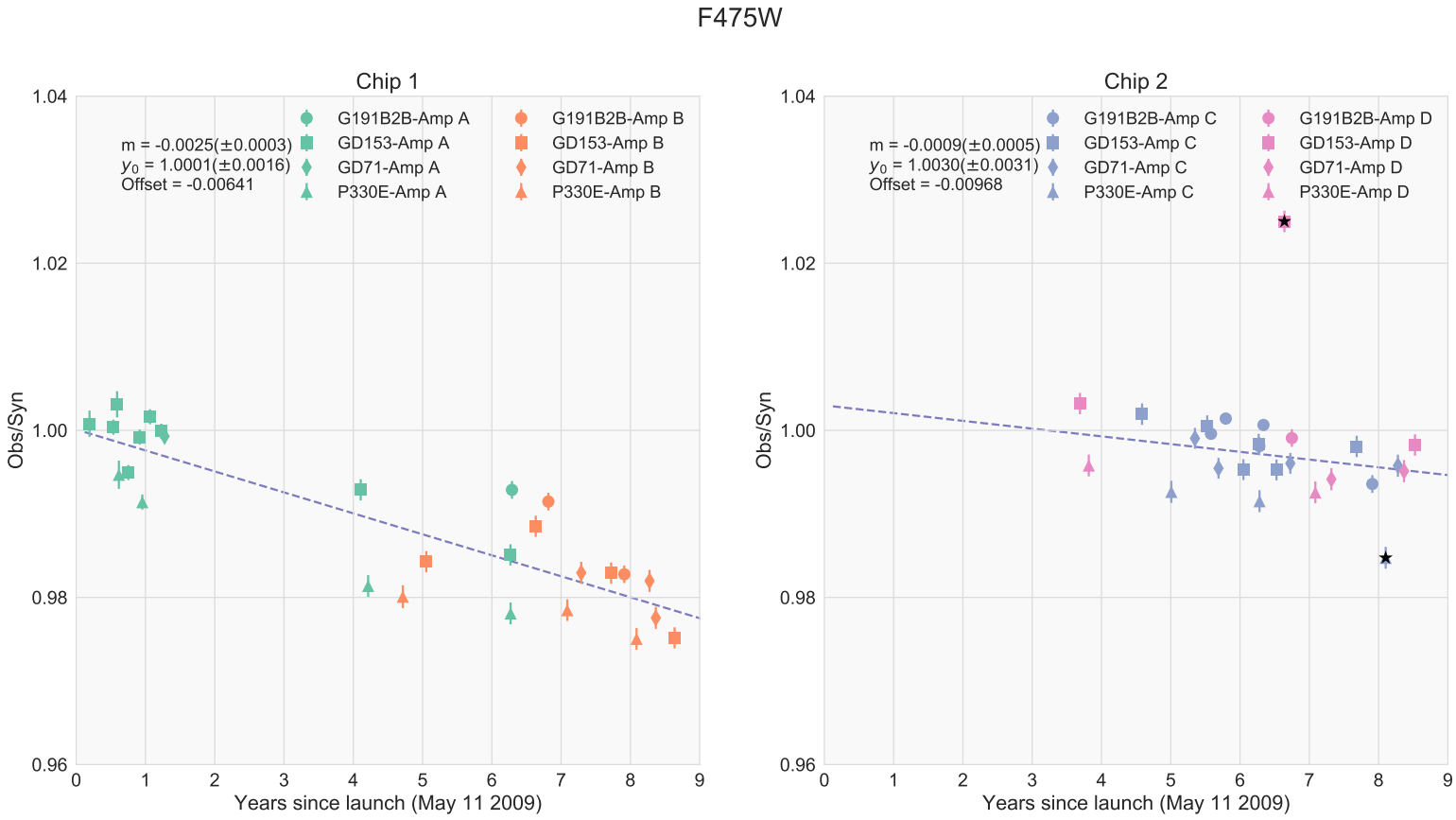

Figure A10: Same as Figure A1 but for F475W

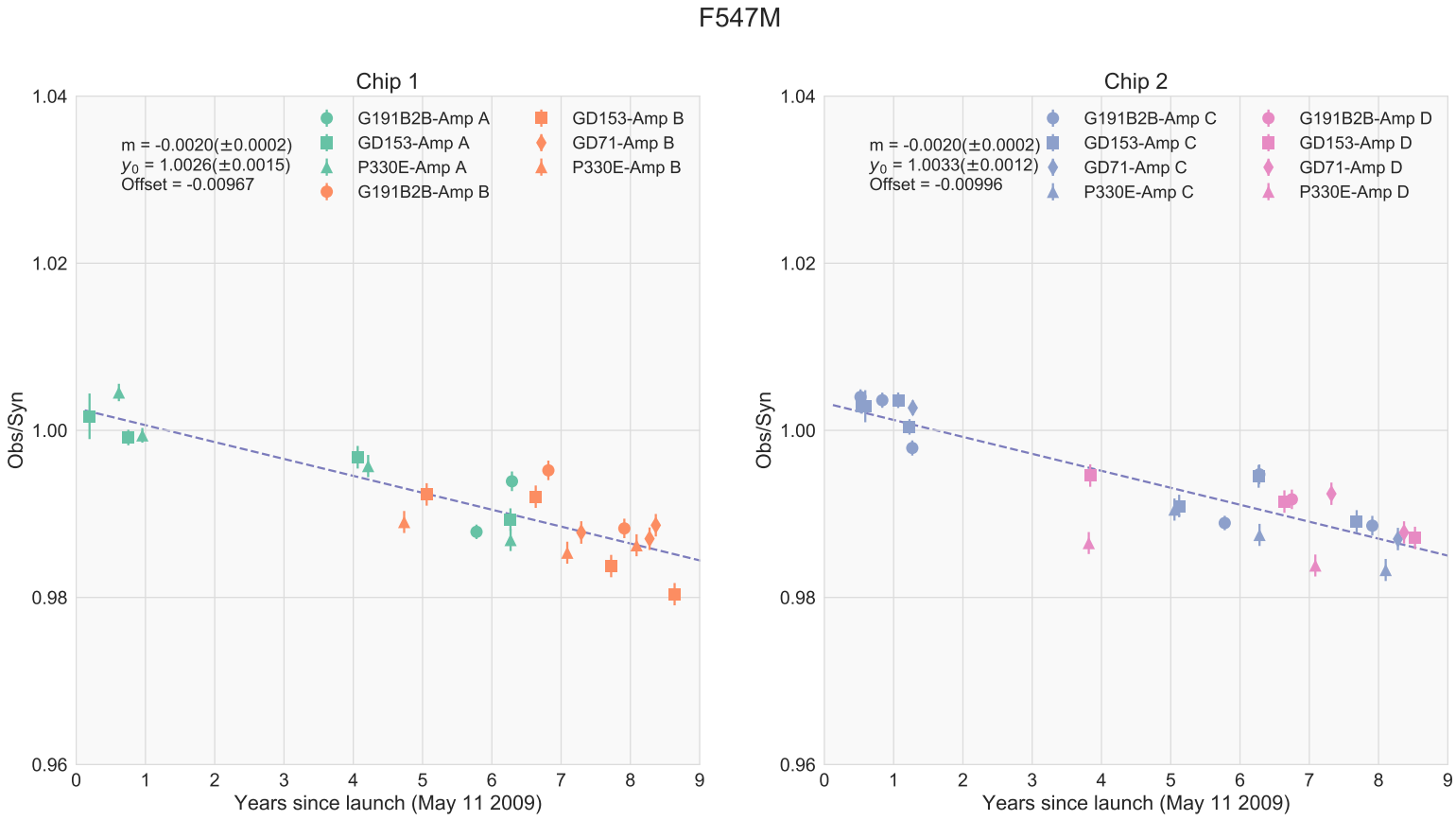

Figure A11: Same as Figure A1 but for F547M

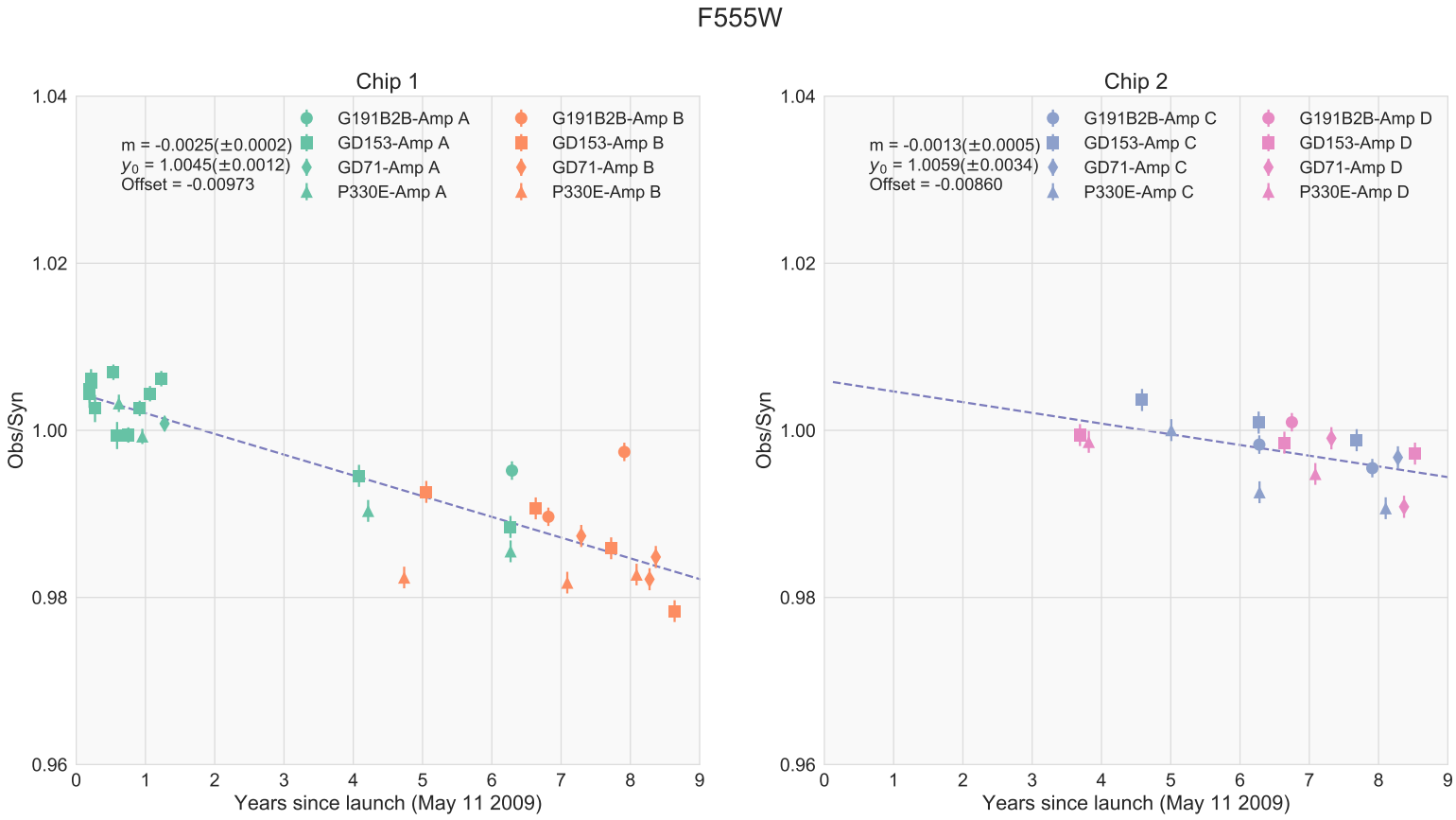

Figure A12: Same as Figure A1 but for F555W

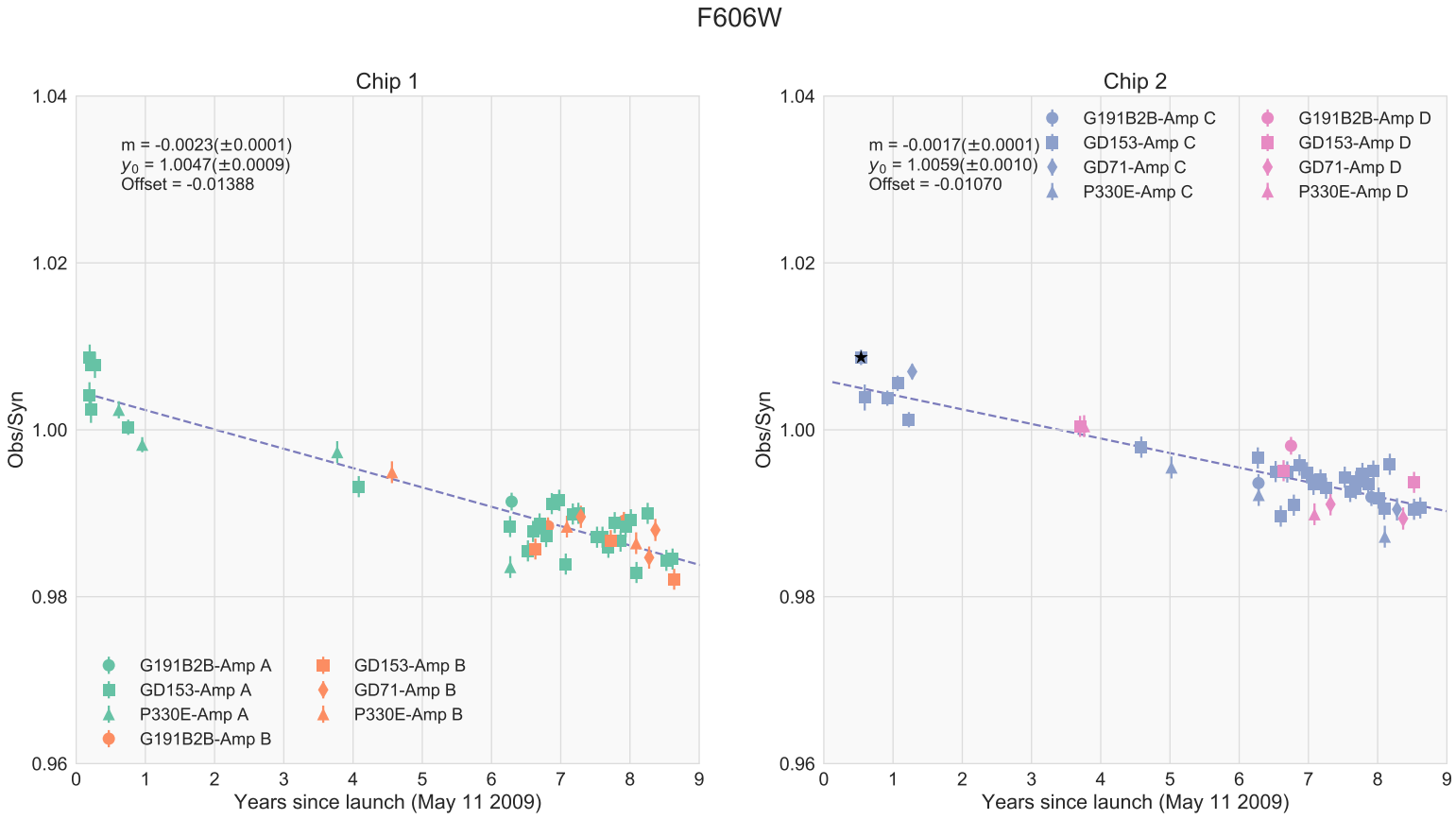

Figure A13: Same as Figure A1 but for F606W

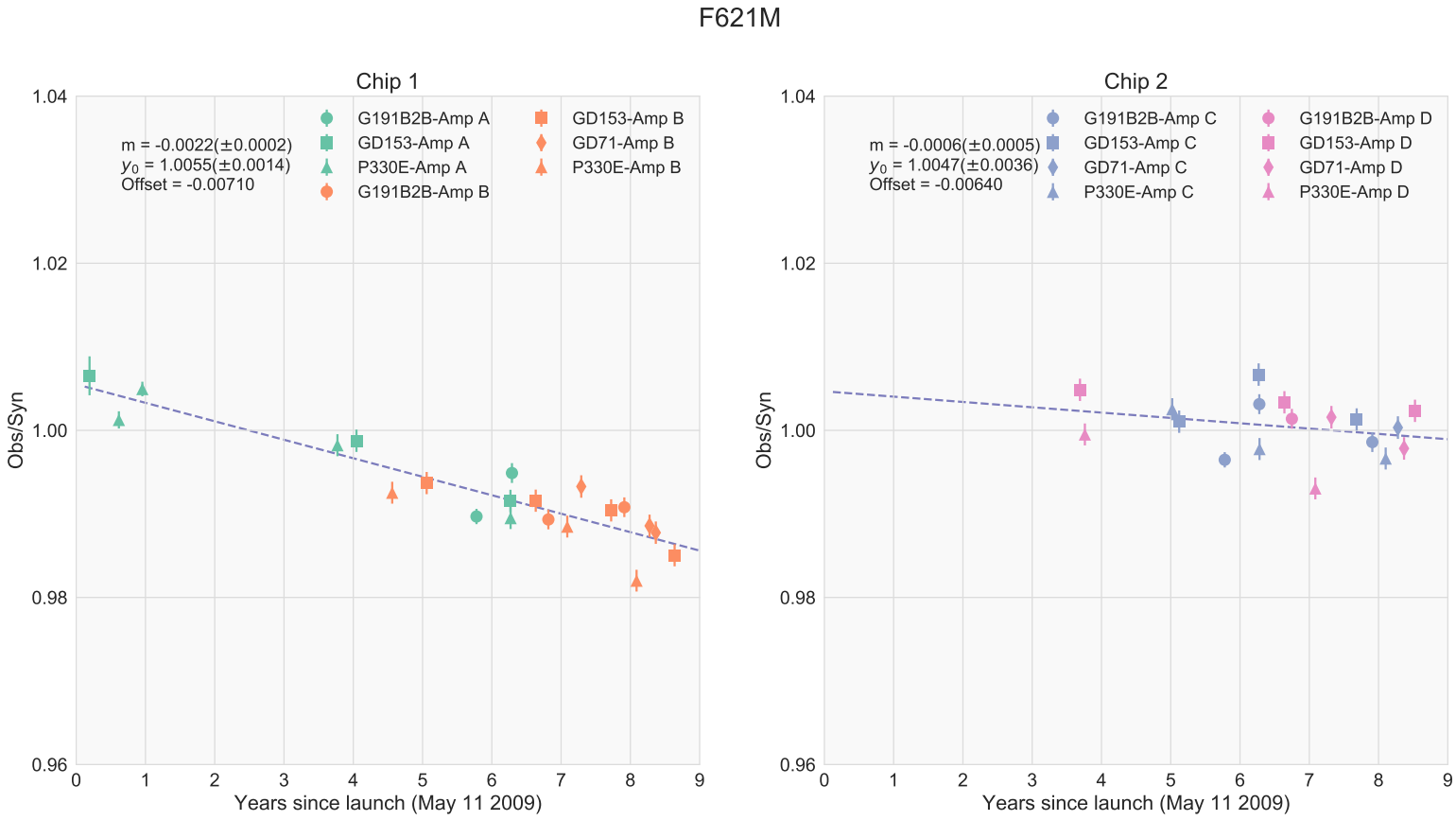

Figure A14: Same as Figure A1 but for F621M

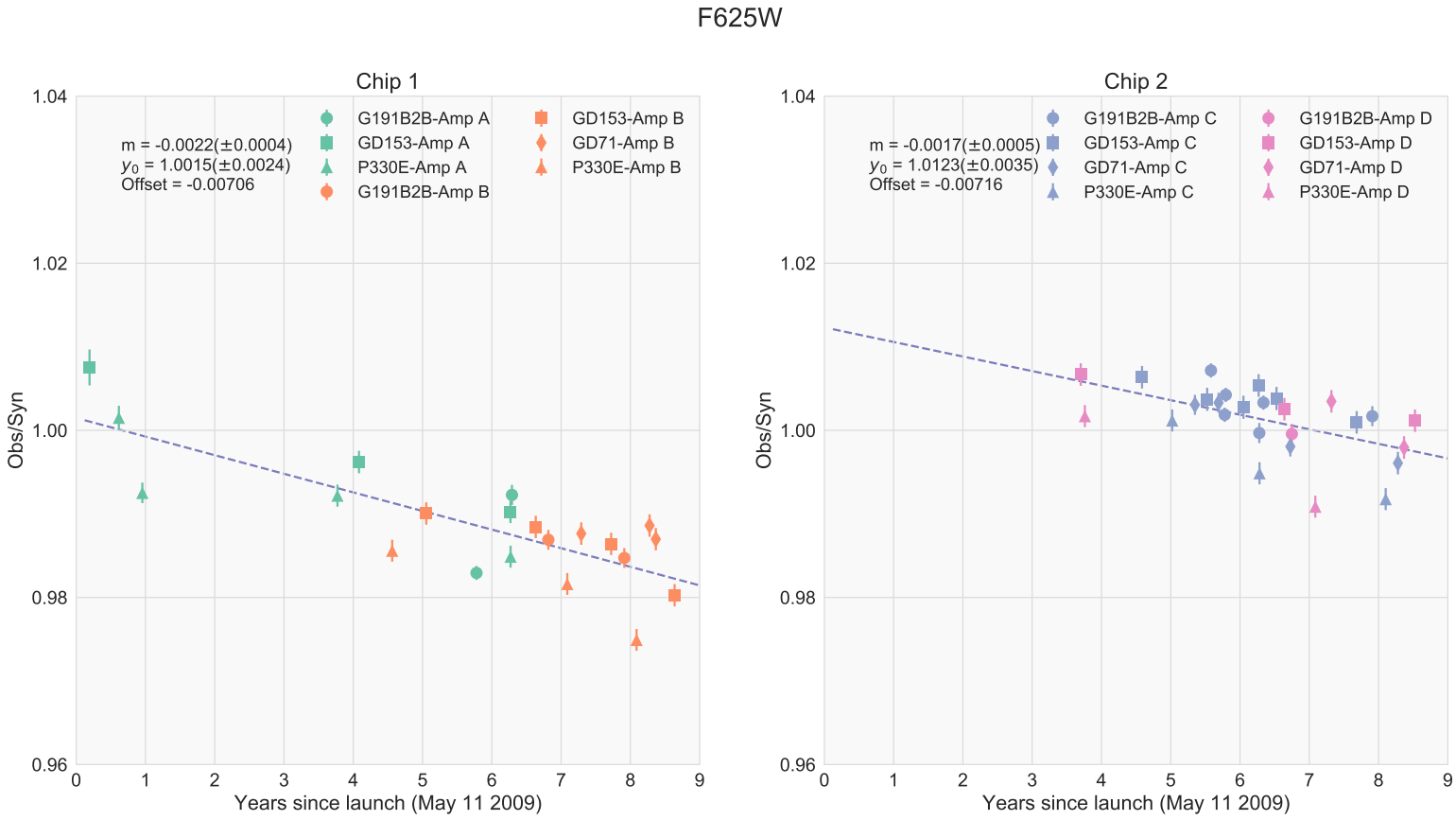

Figure A15: Same as Figure A1 but for F625W

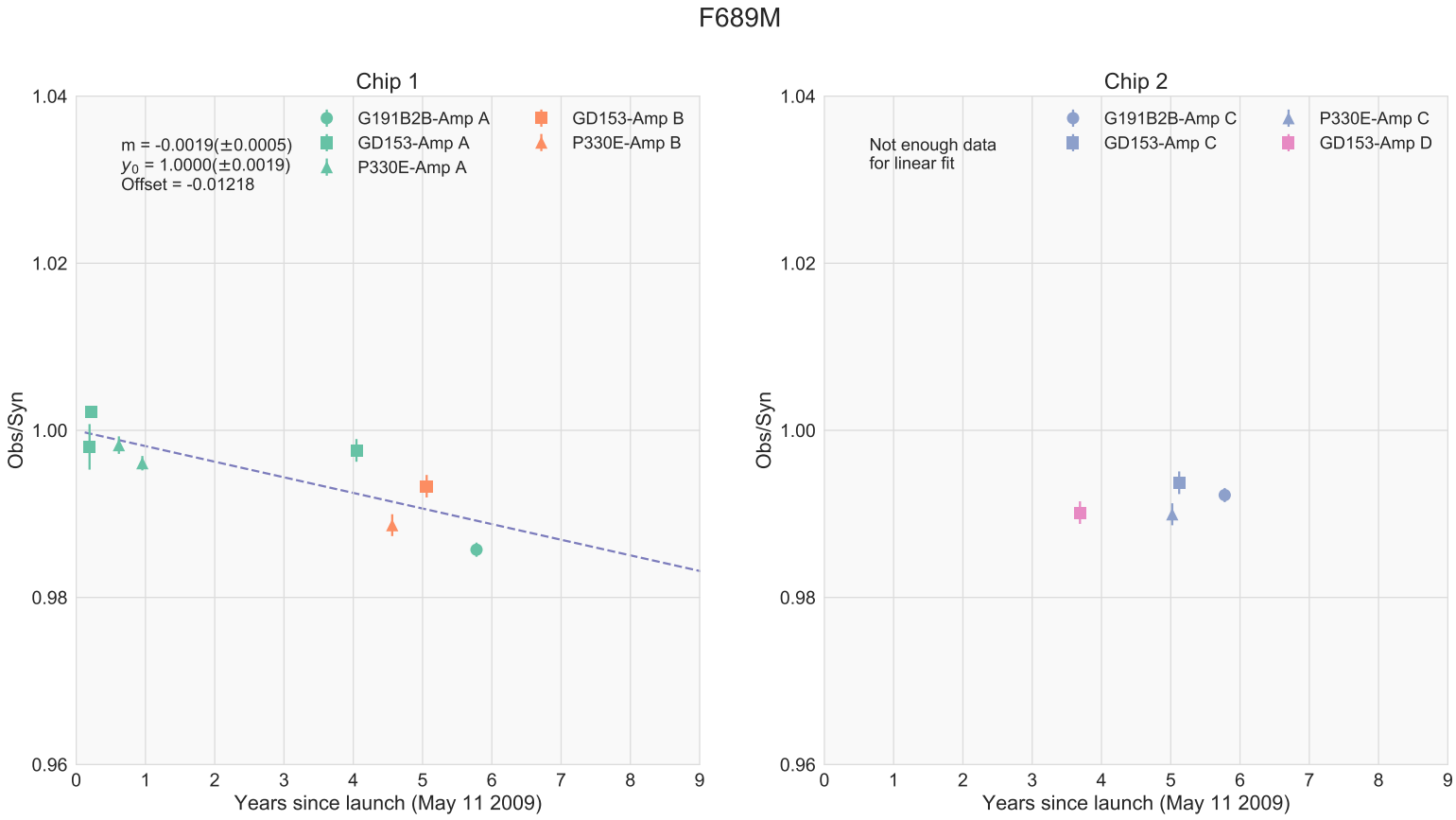

Figure A16: Same as Figure A1 but for F689M

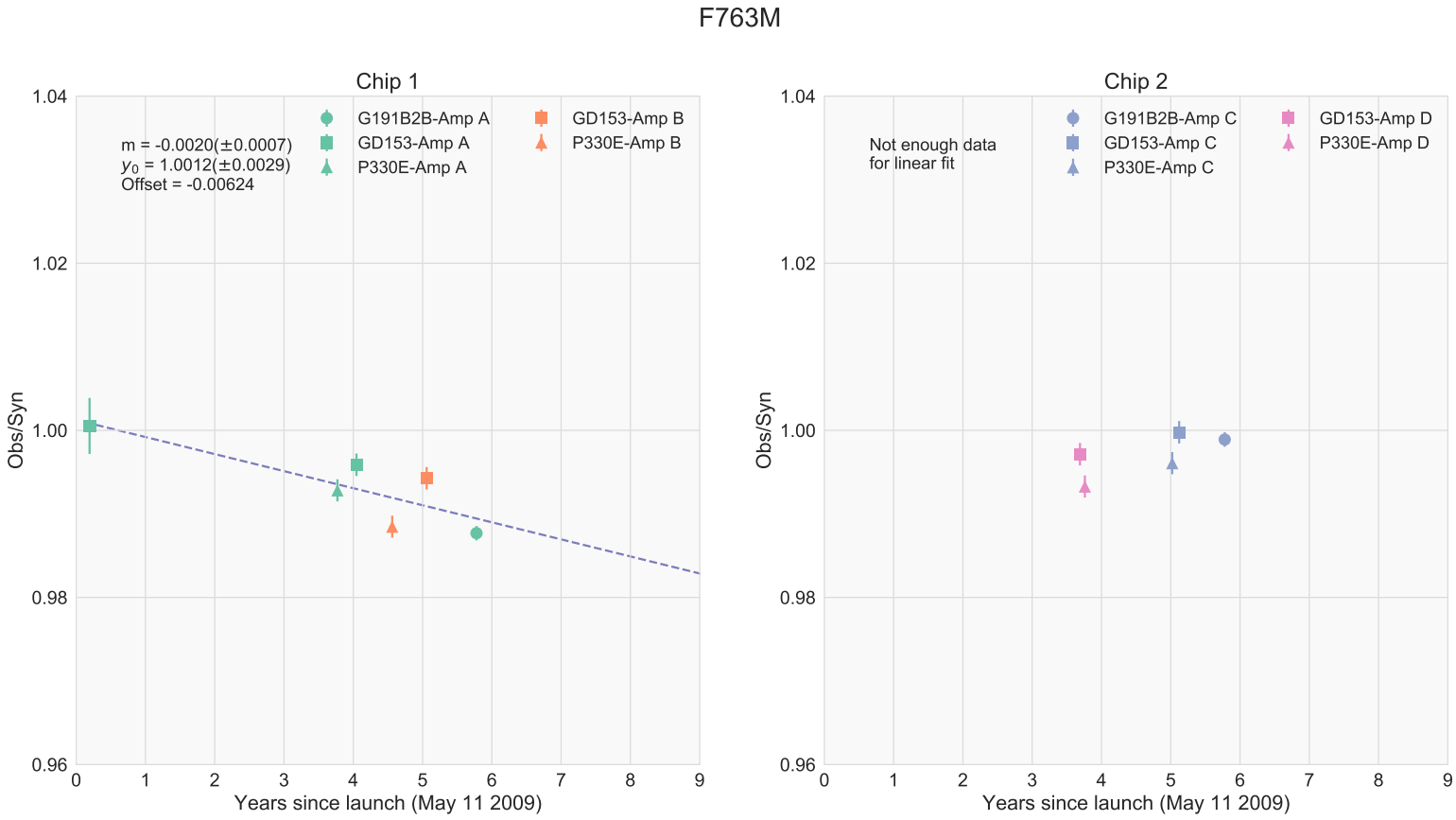

Figure A17: Same as Figure A1 but for F763M

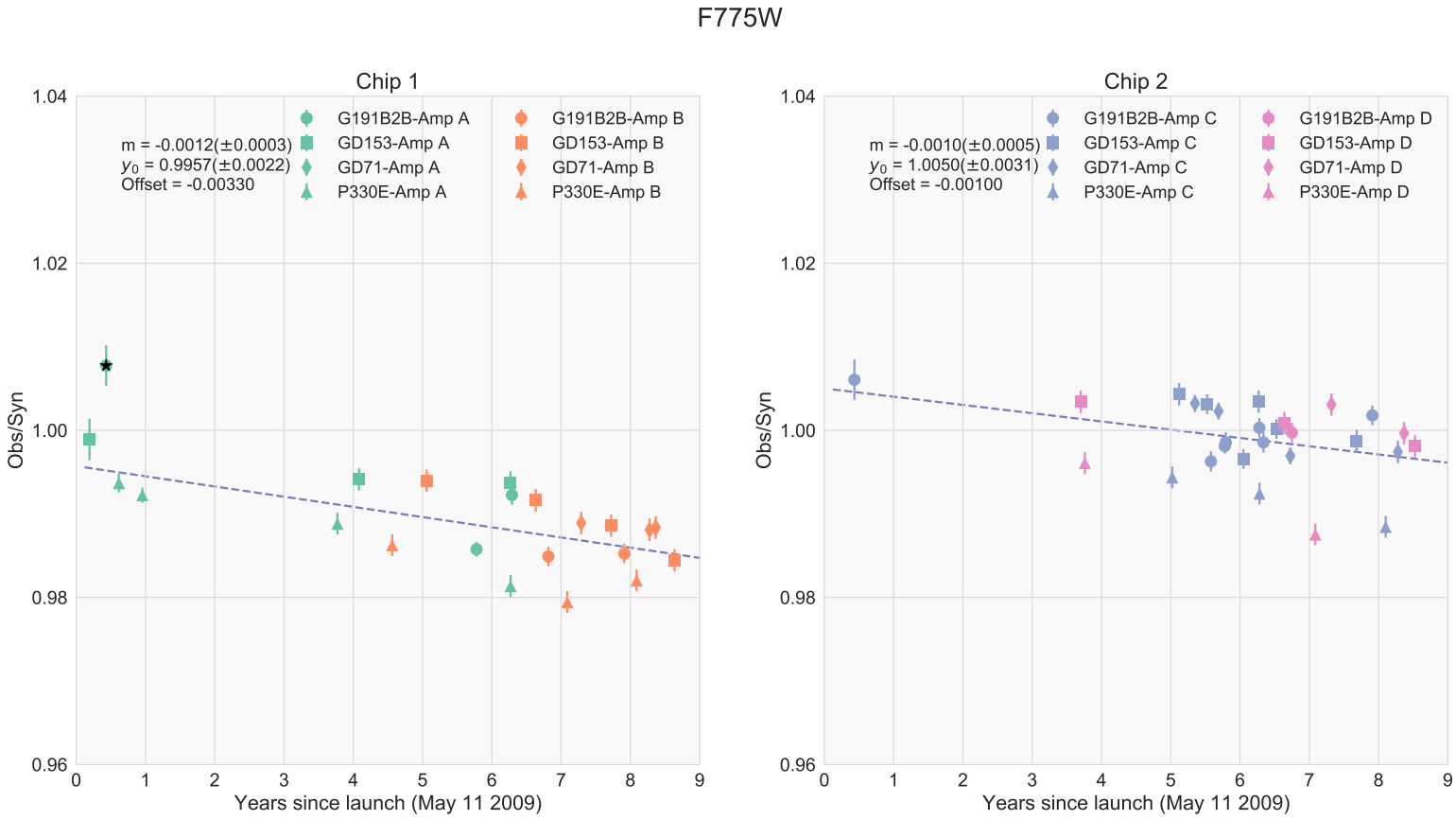

Figure A18: Same as Figure A1 but for F775W

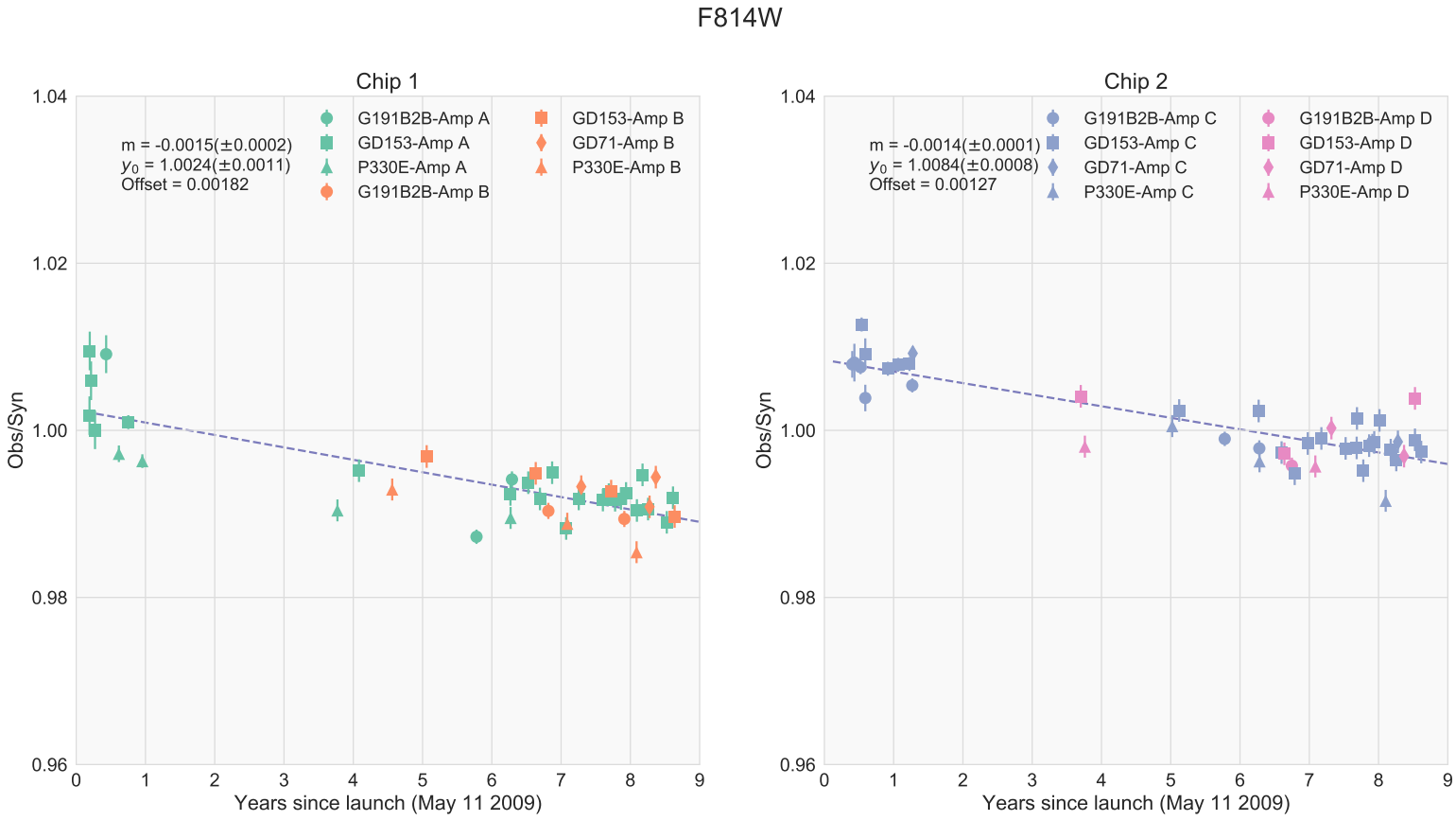

Figure A19: Same as Figure A1 but for F814W

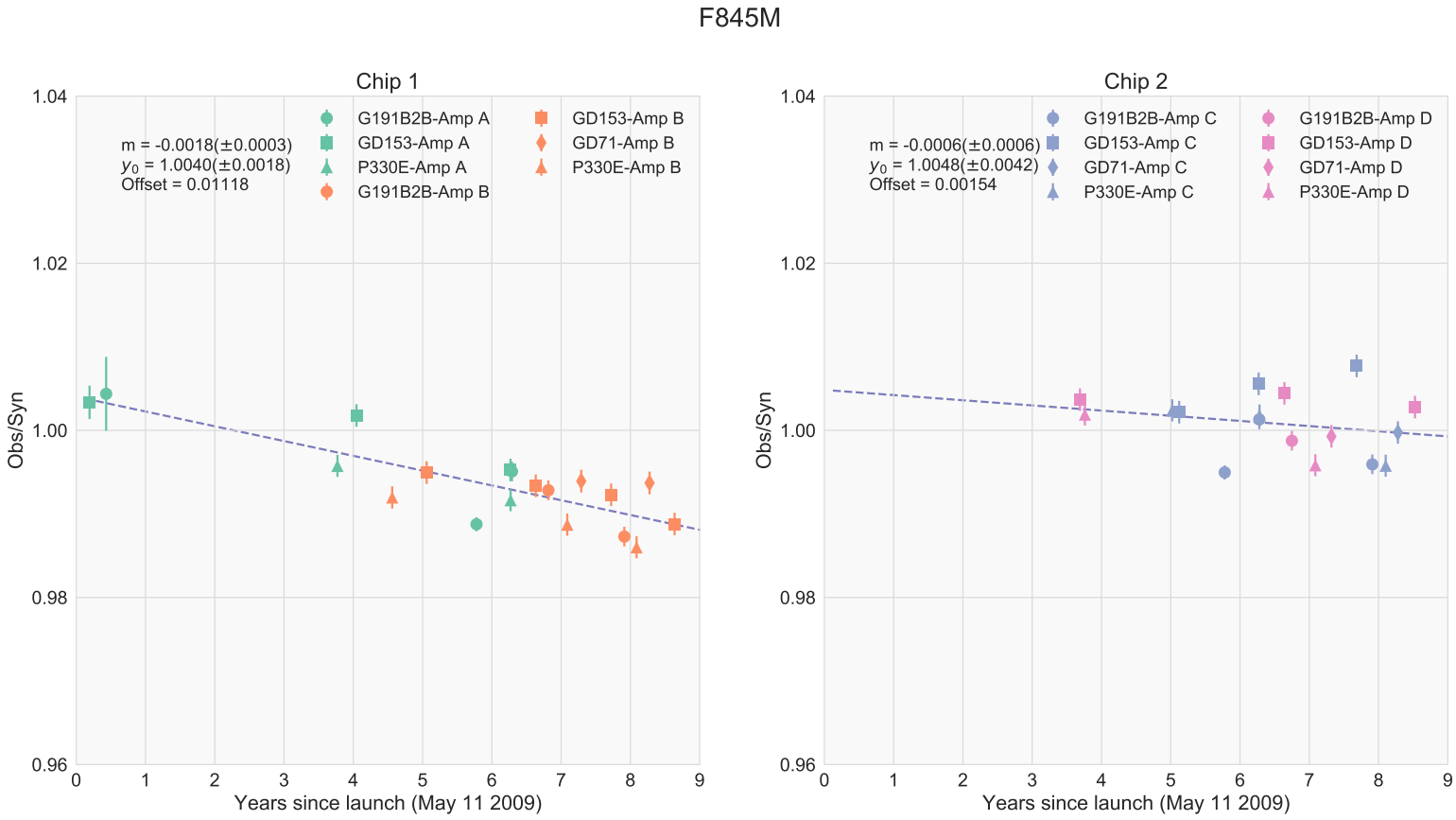

Figure A20: Same as Figure A1 but for F845M

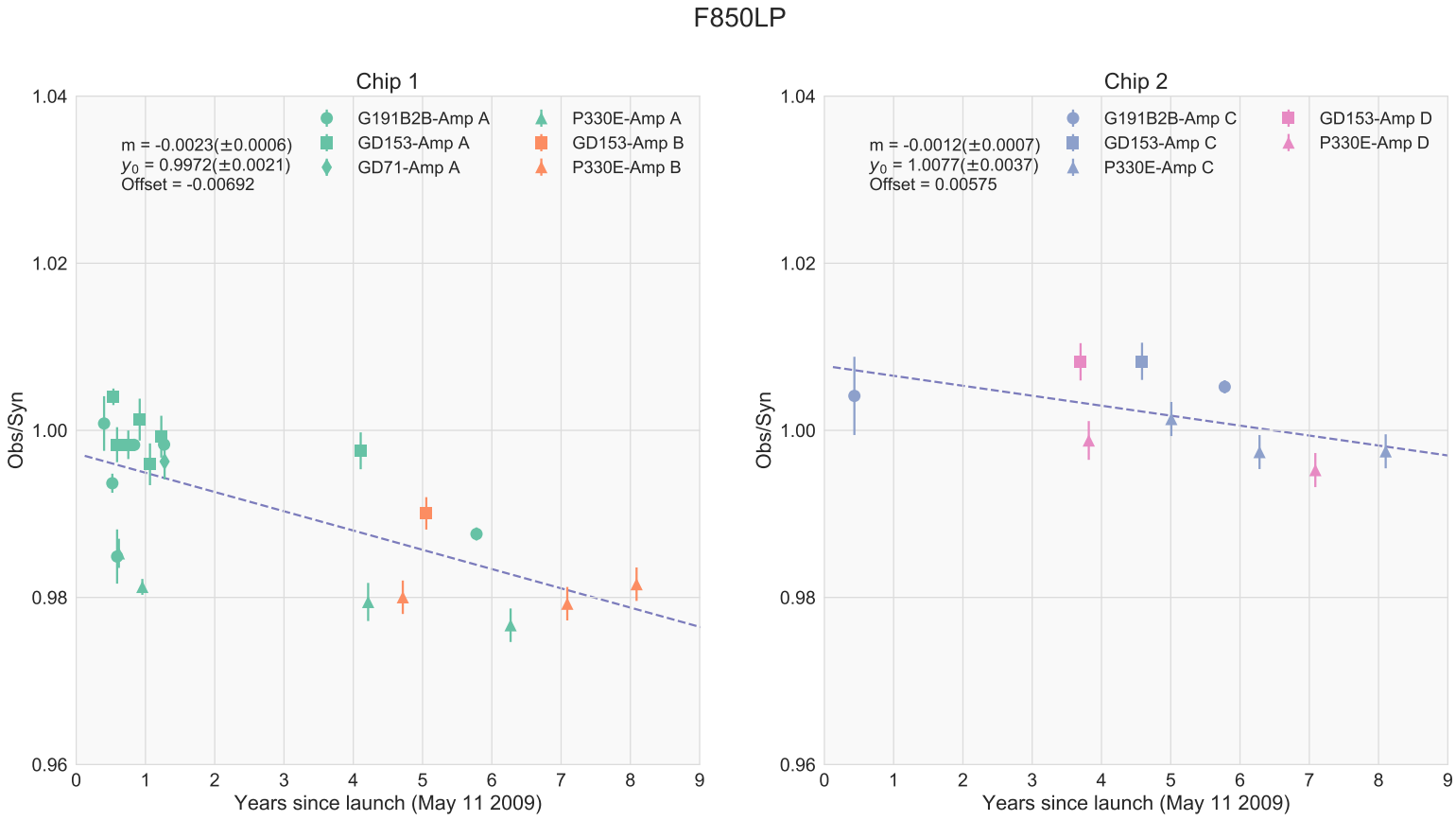

Figure A21: Same as Figure A1 but for F850LP